Entrainment Characteristics of Turbulent Round Gas Jets Submerged in Water

Brady P. Drew

Thesis submitted to the Faculty of the
Virginia Polytechnic Institute and State University
in partial fulfillment of the requirements for the degree of

Master of Science
in
Mechanical Engineering

Pavlos P. Vlachos
John J. Charonko
Sunghwan Jung

July 29th, 2011
Blacksburg, Virginia

Keywords: Entrainment, Multi-phase flow, Particle Image Velocimetry (PIV), Submerged Gas Jets, Spectral Phase Correlation

Entrainment Characteristics of Turbulent Round Gas Jets Submerged in Water

Brady P. Drew

ABSTRACT

The entrainment process in two-phase buoyant jets differs significantly from their single-phase counterparts, and is not well understood. Entrainment models developed for single-phase flow are often used in two-phase jetting simulations, albeit with limited success. In this work, Particle Image Velocimetry (PIV) and shadowgraph flow visualization experiments have been conducted on submerged round gas jets of varying speeds and nozzle diameters with the goal of improving our understanding of the entrainment process in a two-phase (gas-liquid) jet. The total entrainment estimated using the PIV measurements is higher than the respective values suggested by a common empirical model developed for single-phase buoyant jets. A two-phase theoretical entrainment model used for comparison shows an overestimation of entrainment, but predicts the increase in the rate of entrainment with axial distance from the jet nozzle seen in the PIV results.

This thesis also presents advances in PIV processing methodology that were developed concurrently with the entrainment research. The novel Spectral Phase Correlation (SPC) allows for particle displacement to be determined directly from phase information in the Fourier domain. Some of the potential benefits of the SPC explored here include (1) avoidance of errors introduced by spatial peak-finding routines; (2) use of a modal analysis that can be used to provide information such as correlation quality; and (3) introduction of a means of incorporating information from multiple image windows. At low image noise levels, the method performs as well as an advanced CC-based method. However, difficulties unwrapping the aliased phase information cause the SPC's performance to degrade at high noise levels.

This work was supported in part by the Naval Surface Warfare Center (NSWC), Dahlgren Division.

Acknowledgments

I would like to thank the following individuals for their guidance and support:

- Dr. Vlachos for recognizing potential in me as an undergraduate, and pushing me to become a better, more confident, engineer. I feel very privileged to have worked on the projects, and with the people, you bring together in the AEThER lab.
- Dr. Charonko and Dr. Jung, for helping guide my staggering research path and being available to talk whenever I got stuck.
- The Naval Surface Warfare Center, Dahlgren Division, which provided funding for me throughout much of my time in graduate school.
- My parents, for all the love and support you've given me over the years. You've always pushed me to do my best, and have been a great source of inspiration and encouragement.
- My wife, Katie, for moving so far from home, tolerating my long hours at work, and pretending to be interested in Particle Image Velocimetry. Coming home to my best friend gives me at least one good thing to look forward to every day.
- All my labmates, but especially Sam Raben, Nick Cardwell, Chris Weiland, Dave Hubble, and Dan Holden, for all your assistance running experiments, processing data, helping me find (and learn from) my mistakes, and keeping Katie and me off the streets. Your kindness and friendship will certainly be missed.

Contents

List of Figures

List of Tables

Chapter 1

Entrainment by Submerged Gas Jets

1.1 Introduction

The study of buoyant jets has numerous real-world applications, ranging from industrial mixing to environmental flows. The source of the jet, be it a damaged oil well, a natural undersea vent, or a nozzle injecting gas into molten metal, produces a turbulent, momentum-driven flow. Entrainment occurs as the jet interacts with its surroundings, accelerating ambient fluid to the jet's speed. This process is relatively well understood in single-phase flow, such as a smokestack or undersea vent, where the jet and its surroundings are free to mix with one another. However, estimating the rate of entrainment can become significantly more complex when the jet and its surroundings are immiscible. The damaged oil well, for example, ejects crude oil and gas into an aqueous environment. Because none of these three phases are soluble within each other, the continuous jet becomes a complex mixture of water, gas bubbles, and oil droplets. An accurate model of entrainment is essential when simulating these complex multi-phase flows. However, it is often estimated using a model developed for single-phase flows that fails to take into account the effects of immiscibility and high density ratios between the ambient fluid and the jet.

The definition of entrainment for single-phase jets, as found in the literature, is relatively straightforward. In the early work by Morton et al., it is defined as "the inflow into the edge of a convective plume," [3] where the edge of the plume could be defined by a velocity or con-

centration half-width. However, defining entrainment in a two-phase flow comprised of a gas jet submerged in liquid is complicated by the immiscibility between the jet and ambient fluid, and the resulting interfacial dynamics. If Morton et al.'s single-phase entrainment definition was applied to an underwater gas jet, it would imply that only liquid droplets that breach the gas-liquid interface and travel inside the gas column could be considered "entrained." However, there may also be a significant amount of ambient liquid accelerated to the jet's speed that would be considered inside the jet boundary in a velocity- or concentration-based definition of jet width, which would be neglected using such an entrainment definition. In a more recent study, Morton revised the original wording to apply to a wider range of flows:

> *. . . we may need to consider two kinds of entrainment, convective entrainment, which is the response to vortex structures on the scale of the entraining flow, and diffusive entrainment, which is a response to surface turbulence (or surface viscous diffusion), although it is possible that the latter may serve as a detail of the former.* [4]

Similarly, it is hypothesized here that a submerged gas jet will entrain liquid through two distinct mechanisms. In the context of this work, *shear entrainment* refers to droplets entrained into the gas column through surface turbulence. *Advective entrainment* refers to liquid accelerated to the jet's speed, but which is still part of a continuous phase with the ambient environment.

It is hypothesized that shear entrainment is driven by the Kelvin-Helmholtz (KH) instability, which is prevalent in shear flows. This instability occurs when a high shear velocity causes unstable waves to grow on the interface, and is commonly seen in atmospheric flows such as ocean waves or cloud formations. The effect of the KH instability on entrainment by an underwater gas jet is illustrated in Figure 1.1. A high gas velocity parallel to the gas-liquid interface will perturb the boundary, leading the growth of unstable KH waves. As the waves continue to grow, droplets of liquid pinch off and travel inside the gas jet.

The Rayleigh-Taylor (RT) instability is hypothesized to be the driving mechanism behind advective entrainment. The RT instability occurs in density-stratified environments, where interfacial acceleration leads to the formation of finger-like structures. The effect of the RT instability on an underwater gas jet is illustrated in Figure 1.2. Buoyant forces and pressure

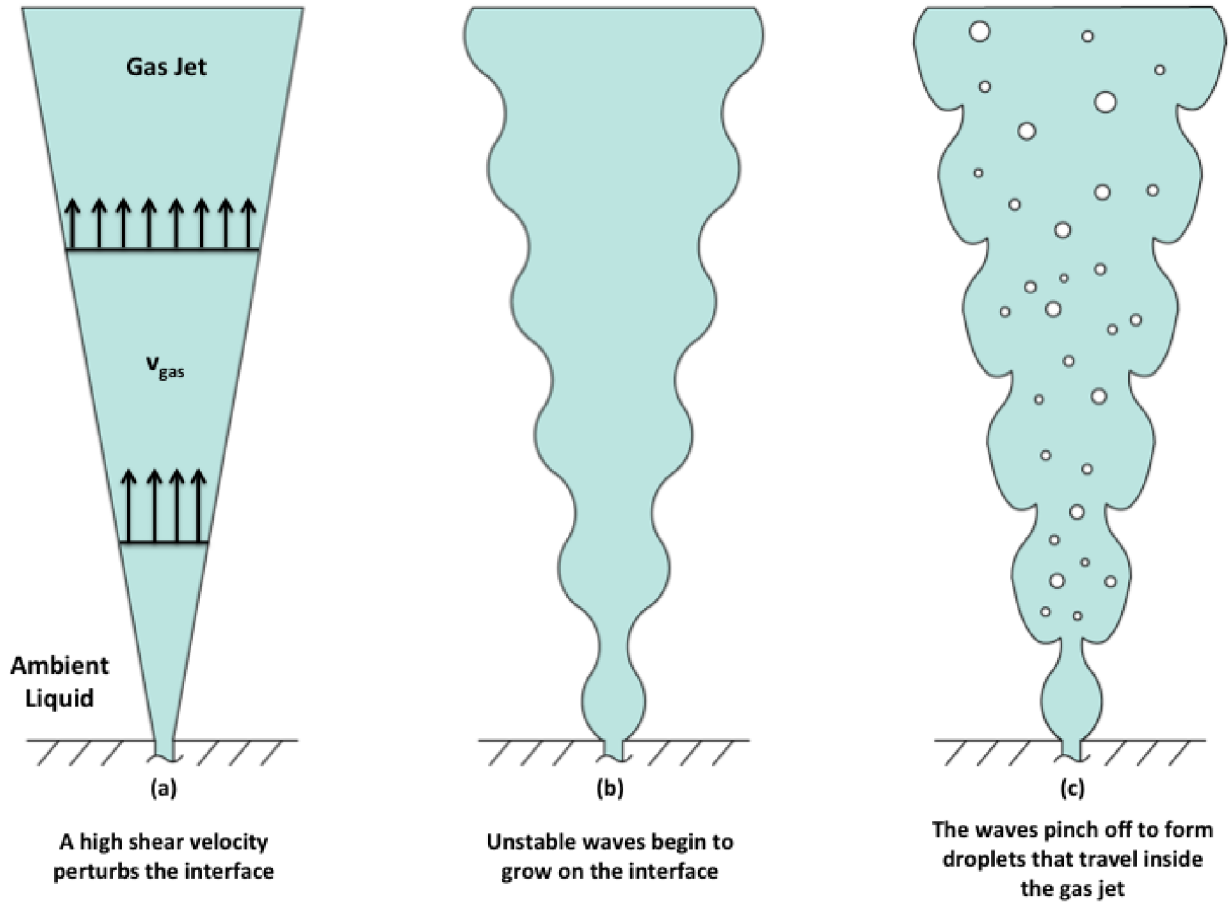

Figure 1.1: Illustration showing the effect of the Kelvin-Helmholtz instability on the entrainment process in an underwater gas jet.

fluctuations inside the jet accelerate the gas-liquid interface radially, causing a wave pattern to form. As the waves grow, some form fingers that pinch off into droplets and are carried along with the gas jet, while others approach the jet centerline and cause the gas column itself to pinch off. These pinch-off events cause significant advective entrainment as ambient fluid fills the area where the gas column no longer exists.

1.2 Background

Early entrainment studies generally concentrated on single-phase buoyant jets. Morton et al. injected a dyed pure water jet into a stratified saltwater environment and estimated

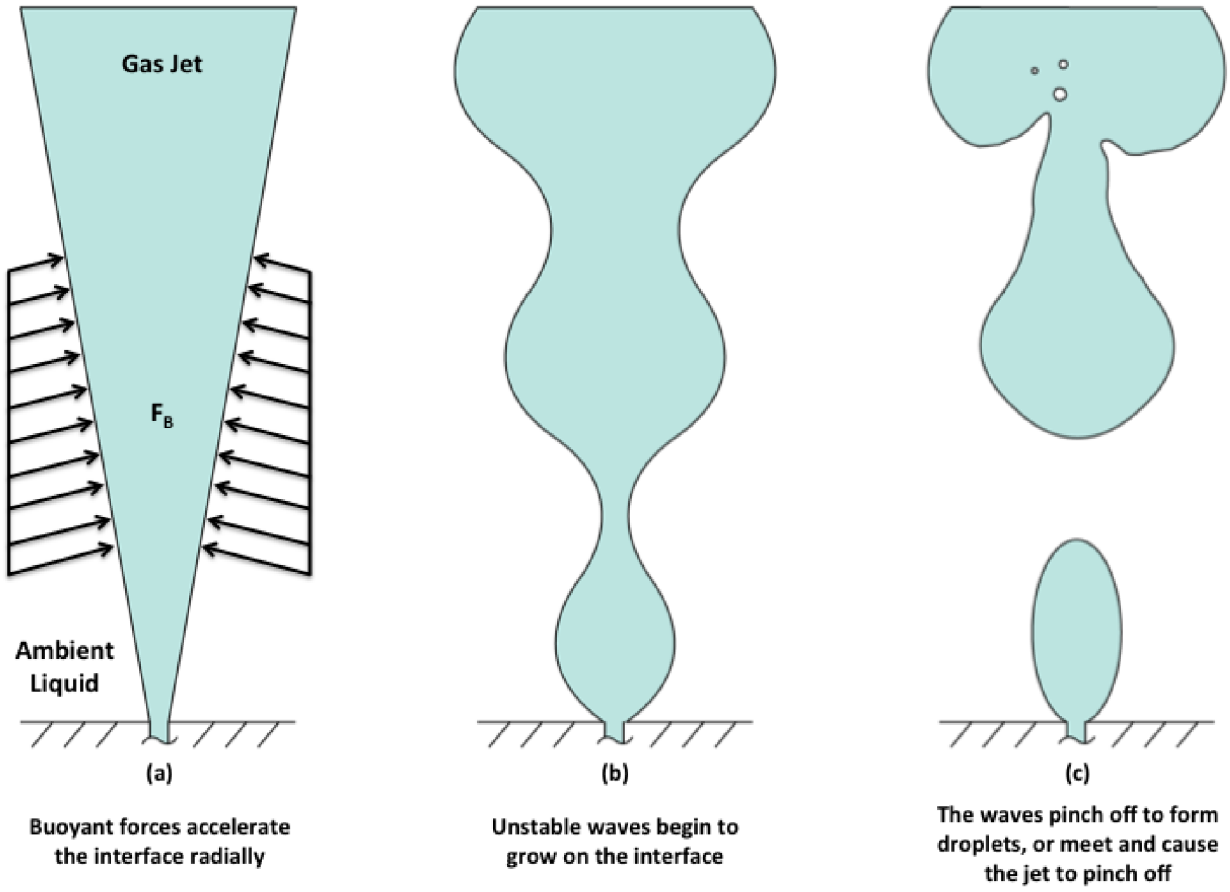

Figure 1.2: Illustration showing the effect of the Rayleigh-Taylor instability on the entrainment process in an underwater gas jet.

entrainment by observing the level to which the dye mixture rose [3]. A linear relationship between entrainment and jet flow rate was found. Ricou and Spalding studied buoyant gas jets in a quiescent gas environment [5], which allowed for a wider range of density ratios than the experiments of Morton et al. Entrainment was quantified using an apparatus that surrounded the jet and measured the flow rate of air required through the apparatus in order to maintain a neutral pressure gradient. They found a linear relationship between jet flow similar to that of Morton et al., but proposed an expanded entrainment model, which, in

addition to flow rate, also took into account the densities of the jet and ambient fluid:

$$\frac{\dot{m}}{\dot{m}_0} = C_2 \frac{y}{d_0}\sqrt{\frac{\rho_f}{\rho_g}} \tag{1.1}$$

$$\dot{m} = \dot{m}_0 + \dot{m}_{ent} \tag{1.2}$$

$$C_2 = \frac{d\left(\dot{m}/\dot{m}_0\right)}{dy} d_0 \sqrt{\frac{\rho_g}{\rho_f}} = \frac{d\dot{m}_{ent}}{dy}\frac{d_0}{\dot{m}_0}\sqrt{\frac{\rho_g}{\rho_f}} \tag{1.3}$$

where $\dot{m}$ is the mass flow rate of the jet, the 0 subscript refers to conditions at the nozzle exit, the *ent* subscript refers to entrainment, y is the axial distance from the nozzle, d_0 is the nozzle diameter, and ρ_f and ρ_g are the densities of the ambient fluid and gas, respectively. C_2 is an empirical constant (0.32 in Ricou-Spalding's experiments) describing the rate of change of jet flow rate with axial distance. It is referred to throughout this study as the *entrainment coefficient*.

Hill performed similar buoyant gas jet experiments, but concentrated on the region of the jet closest to the nozzle [6]. He found that Ricou-Spalding's linear relationship did not hold in this initial region, and proposed using lower values for the entrainment coefficient at axial distances less than 13 diameters, decaying to 0 at the nozzle exit.

Weimer and Faeth were among the first to study entrainment in two-phase jets [7]. A horizontal steam jet was injected into various liquids at high enough speeds that buoyancy effects could be neglected. Entrainment was estimated by measuring the penetration of the jet into the liquid bath. Their results showed a higher entrainment coefficient than Ricou-Spalding's experiments, but they claim "reasonable agreement" given the vastly different density ratios between the two studies.

Tross studied gas jets submerged in water [8] using a continuity probe to detect void fraction, and dynamic pressure measurements to determine velocity throughout the flow field. Based on the experimental results and a theoretical formulation introduced by Morton et al. [3, 9], Tross proposed equations to describe the mean properties of a submerged gas jet as a function of axial and radial distance from the nozzle. The experiments showed a slightly lower entrainment coefficient than Ricou-Spalding, but it is concluded that, "...two-phase jets are similar to single-phase jets with regard to entrainment, when proper allowance is

made for variable density effects in these flows." [8]

Loth and Faeth used Laser Doppler Velocimetry (LDV) to measure velocities in the ambient fluid surrounding an underwater gas jet, and quantified entrainment by determining the flow rate of liquid moving perpendicular to the mean gas interface [10]. Their results showed reasonable agreement with Ricou-Spalding at high flow rates or near the nozzle. However, they found higher rates of entrainment than the model would predict as the flow rate decreased or axial distance from the nozzle increased.

All these previous studies of two-phase jets make a comparison with Ricou-Spalding's single-phase entrainment model, albeit with limited success, as there are significant physical differences between a gas jet in liquid and single-phase jets. Ricou-Spalding's model attempts to correct for the density difference between the jet and its surroundings, but the density ratio for a gas jet in liquid is two orders of magnitude higher than the highest ratios studied in a gaseous environment. Surface tension and the dynamic behavior of the interface between the gaseous and liquid phases is another factor not taken into account in a single-phase entrainment model. Since the jetting fluid and the ambient fluid are immiscible, the jet cannot mix with the ambient environment without the occurrence of pinch-off events.

Epstein et al. developed a theoretical model for two-phase jet entrainment, which takes into account both surface tension and large density ratios [11]. The model assumes that entrainment is due to a combination of RT and KH instabilities growing on the gas-liquid interface. An equation for the linear growth of a two-dimensional surface wave due to KH and RT instabilities as a function of wavenumber was maximized in order to find the fastest-growing wave. The study then assumed that droplets would pinch off from the gas-liquid interface at a length scale equal to one half of the fastest-growing wave's wavelength, in order to obtain an approximation of entrainment per unit of interfacial area, $\dot{m}''_{ent}$, due to a combination of both RT and KH instabilities:

$$\dot{m}''_{ent} \approx \frac{1}{\sqrt{3}} \left(\rho_g \rho_f\right)^{1/2} v \sqrt{\frac{6\Psi}{1 + \left(1 + 3\Psi\right)^{1/2}} + 1} \tag{1.4}$$

This analysis introduces Ψ, a nondimensional parameter relating the relative importance of the RT instability to the KH instability, defined as:

$$\Psi = \frac{\sigma a \rho_f}{\rho_g^2 v^4} \tag{1.5}$$

where σ is the surface tension, a is the acceleration normal to the interface, and v is the axial velocity of the gaseous phase at the interface. As the surface tension and interfacial acceleration terms become more significant than the shear velocity, Ψ will become much greater than 1. The RT instability will dominate and the entrainment approximation will reduce to:

$$\dot{m}''_{ent} \approx \sqrt{\frac{2}{3}} \left(\frac{3\sigma a}{\rho_f} \right)^{1/4} \rho_f \tag{1.6}$$

Note that this asymptotic solution is very different from previous entrainment models in that it incorporates surface tension and is independent of jet velocity. At high shear velocities, Ψ will be much less than 1 and the KH instability will dominate:

$$\dot{m}''_{ent} \approx \frac{1}{\sqrt{3}} \left(\rho_g \rho_f \right)^{1/2} v \tag{1.7}$$

The KH asymptote of the Epstein model is remarkably similar to the Ricou-Spalding model in that it incorporates a constant, densities, and the jet speed, while neglecting surface tension and interfacial acceleration. However, note that the Epstein model requires information about the jet dynamics as a function of height, while the Ricou-Spalding model requires only initial conditions at the nozzle exit.

Epstein et al.'s work concentrated on energetic core disruptive events in nuclear reactors, and it was assumed that the entrainment process was dominated by the KH instability because of the high gas velocities in such an event. However, the relative importance of RT and KH instabilities in other types of submerged gas jets has not been thoroughly examined, and it is unknown if their model will apply over a wide range of flow parameters.

1.3 Methods

1.3.1 Experimental Facilities and Techniques

Experiments were conducted in the Advanced Experimental Thermofluids Engineering Research (AEThER) Laboratory at Virginia Tech. Shadowgraph images were acquired in order to obtain information about the gas-liquid interface dynamics, study the jet dynamics, and provide inputs for the Epstein entrainment model. Particle Image Velocimetry (PIV) experiments on the same jet speeds and nozzle diameters were performed to obtain information about the flow field in the ambient liquid. Entrainment was quantified using the PIV data in order to provide an experimental validation of the entrainment models.

The experimental setup for both experiments consisted of a clear acrylic tank with a gas injector assembly flush-mounted to an acrylic plate inside the tank. A fast acting valve was used to impulsively switch on the gas injection, and pressure and temperature sensors were used to monitor relevant parameters throughout the tests. The experiment was controlled using a LabVIEW program to synchronize the gas injection valve with the pressure and temperature sensors and a high-speed camera.

Jet Operation and Instrumentation

The rapid prototyped gas injector assembly, shown in the top right of Figure 1.3, consisted of a common base component that would house different nozzles, which could be interchanged in order to vary the Mach number and jet diameter. Two sets of nozzles were manufactured, with a common exit diameter between the nozzles in a set ($d_0 = 3.175mm$ and $d_0 = 6.350mm$). The throat diameter was varied to achieve properly-expanded jets with exit velocities ranging from Mach 0.4 to Mach 2.1. Rubber O-rings were used to ensure an airtight seal between the base and the interchangeable nozzles. Air for the jet was supplied via five gas injection ports spaced evenly around the circumference at the bottom of the base.

The acrylic tank was filled with untreated tap water. The gas injector assembly was flush-mounted to an acrylic plate located approximately $0.46m$ below the water level in the tank.

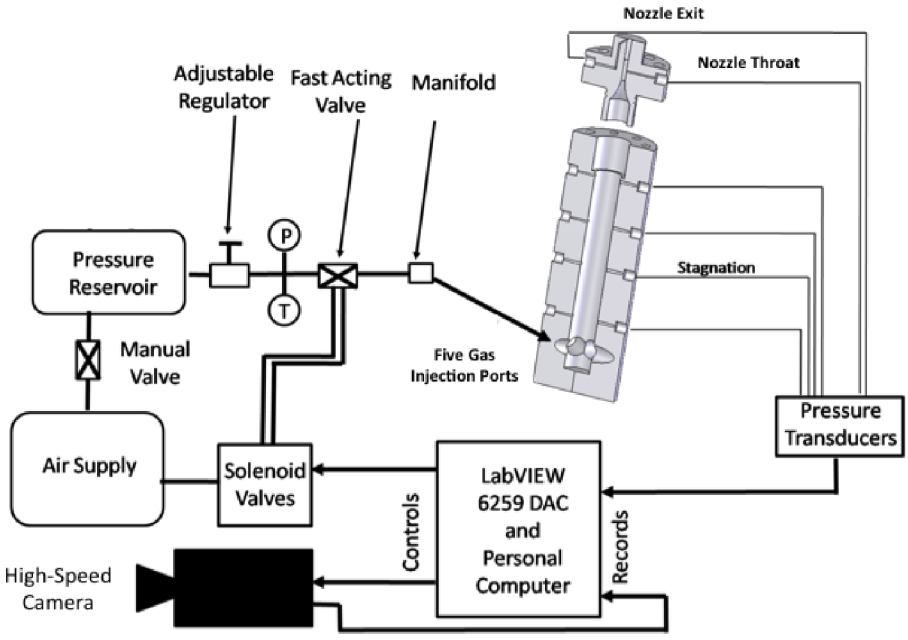

Figure 1.3: Schematic of the jet instrumentation and control system. [1]

A wave breaker constructed from perforated steel sheeting was installed at the water line to limit surface waves, which could cause variations in the hydrostatic pressure. It also had the practical advantages of keeping water from being ejected out of the tank by the gas jet, and forcing the ambient environment to reach a quiescent condition more quickly after each test. Past researchers have shown that wave dampers do little to alter characteristics of the flow [10, 12].

Figure 1.3 shows a schematic of the jet instrumentation and control system, whose function was to deliver a constant flow of air to the nozzle and record data needed to characterize the jet. This system was controlled by a National Instruments data acquisition card, in conjunction with a LabVIEW program developed for this experiment. This allowed for synchronization of the data acquisition with the gas injection and image acquisition by establishing an accurate reference time. To run the system, the software sent a digital signal to the camera to start recording, along with a simultaneous analog signal to the fast-acting gas supply valve. Upstream of this valve, the gas reservoir was connected to a pressure regulator designed to produce a steady output even under changing backpressure, which was

manually adjusted to control the flow rate. The pressure and temperature downstream of the regulator were monitored during the test to ensure that the flow rate remained constant. To monitor the jet during the tests, static and stagnation pressures inside the base, as well as the nozzle throat and exit pressure were recorded using absolute pressure transducers. Mach number was calculated using the isentropic law relating pressure and Mach number. The exit pressure was compared with the hydrostatic pressure (computed by measuring the barometric pressure and recording the water level in the tank) to ensure proper expansion of the jet at the nozzle exit plane.

To keep water in the tank from intruding into the gas delivery system when the jet was not in operation, backflow preventers were installed on the five gas delivery ports at the base of the nozzle, and air was constantly delivered through the pressure lines. When the jet was turned on, solenoid valves were used to quickly shut off this gas flow to allow for accurate pressure measurements. In order to ensure this did not affect computations using the pressure data, the first one second of each test was discarded in order to allow the jet to reach a steady-state condition.

Shadowgraph Data Acquisition and Edge Detection

Shadowgraph experiments were performed to obtain quantitative information about the dynamics of the gas-liquid interface. A high-speed camera (Integrated Device Technologies XS-5) recorded images of the underwater gas jet at a sampling rate of $500Hz$. The $50mm$ Nikon lens used in the experiment produced a resolution of approximately $240\mu m/pixel$. Rather than lighting the jet from behind, as would typically be done in shadowgraph experiments, an array of high frequency fluorescent lights was used to illuminate the jet from the left side of the image frame. This was done so that structures on the gas-liquid interface, which would otherwise be obscured using backlighting, could be visualized in detail. The test matrices for the shadowgraph experiments using the $3.175mm$ and $6.350mm$ exit diameter nozzles are presented in Tables 1.1 and 1.2, respectively. Each test lasted 6 seconds and was repeated five times in order to gauge the repeatability of the results.

The acquired images from each test were processed in MATLAB to track the position of the gas-liquid interface throughout the test. The interface was detected using the process

Table 1.1: Shadowgraph test matrix showing the measured Mach numbers for each of the $3.175mm$ nozzle diameter tests

Design Speed	**Test 1**	**Test 2**	**Test 3**	**Test 4**	**Test 5**	**Mean**	**Std. Dev.**
Mach 0.4	0.417	0.390	0.401	0.408	0.384	0.400	0.013
Mach 0.6	0.602	0.599	0.604	0.593	0.614	0.602	0.008
Mach 0.8	0.807	0.803	0.806	0.815	0.797	0.805	0.007
Mach 1.0	0.965	0.999	0.989	0.988	0.975	0.983	0.013
Mach 1.2	1.102	1.095	1.101	1.090	1.115	1.101	0.010
Mach 1.5	1.589	1.597	1.590	1.585	1.605	1.593	0.008
Mach 1.7	1.887	1.895	1.886	1.881	1.883	1.887	0.005
Mach 2.0	2.094	2.084	2.088	2.081	2.083	2.086	0.005

Table 1.2: Shadowgraph test matrix showing the measured Mach numbers for each of the $6.35mm$ nozzle diameter tests

Design Speed	**Test 1**	**Test 2**	**Test 3**	**Test 4**	**Test 5**	**Mean**	**Std. Dev.**
Mach 0.4	0.402	0.393	0.405	0.392	0.412	0.401	0.008
Mach 0.6	0.601	0.603	0.596	0.602	0.588	0.598	0.006
Mach 0.8	0.788	0.806	0.801	0.780	0.807	0.800	0.008
Mach 1.0	0.988	0.988	0.991	0.964	0.980	0.982	0.011
Mach 1.2	1.335	1.330	1.311	1.332	1.329	1.327	0.010
Mach 1.5	1.649	1.644	1.651	1.649	1.650	1.649	0.003
Mach 1.7	1.850	1.846	1.844	1.845	1.844	1.846	0.003
Mach 2.0	2.135	2.130	2.136	2.135	2.135	2.134	0.002

illustrated in Figure 1.4. First, a high-pass Gaussian filter was applied to the original images to remove low-frequency noise and improve contrast between the jet and the background. The filtered images were then binarized using a threshold pixel intensity, which was varied

slightly between tests to ensure accurate detection of the gas phase. A median filter and a morphological dilate/erode function (using a disk-shaped element) were applied to the binarized images with the goal of smoothing out noise caused by poor illumination or gas bubbles not attached to the jet. Finally, a perimeter search was performed to locate the boundary of the gaseous region. As seen in the final frame of Figure 1.4, this process worked well in detecting the jet interface without including a significant amount of extraneous gas.

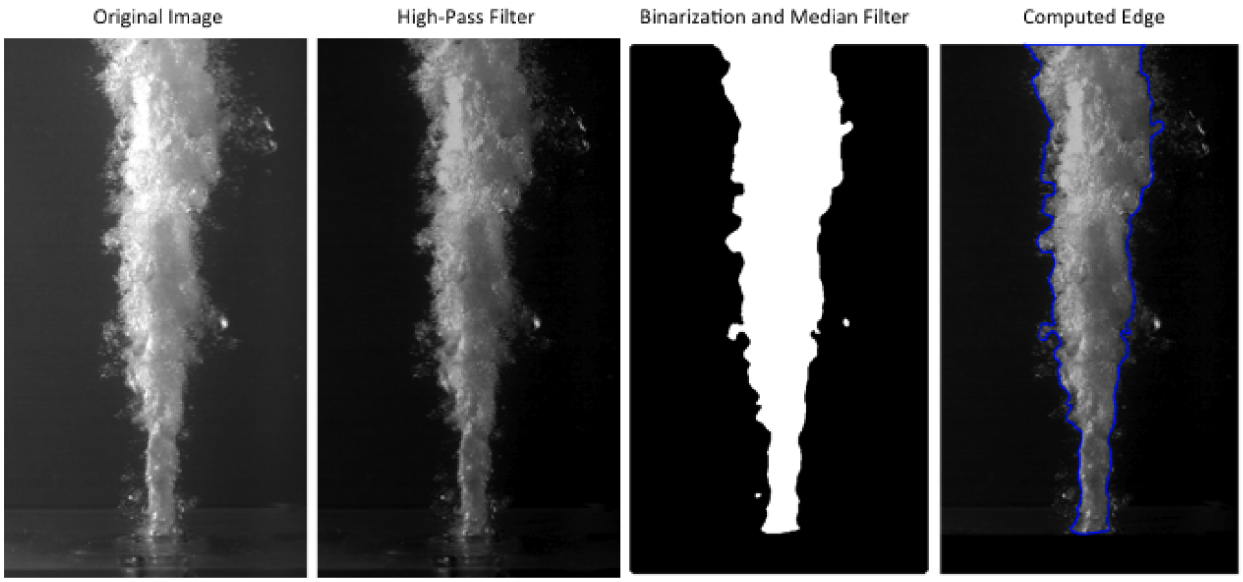

Figure 1.4: Processing steps used to detect the jet boundary from shadowgraph images.

Particle Image Velocimetry Experiments

Particle Image Velocimetry (PIV) is an experimental technique that can be applied to a wide range of fluid flows to produce quantitative information about fluid velocity [13]. PIV data was collected on the underwater gas jet to gain insight into the movement of the ambient fluid, from which conclusions about entrainment could be drawn. A schematic of the experimental setup is shown in Figure 1.5. It consisted of a Photron Fastcam APX RS high-speed camera with a $50mm$ Nikon lens ($f\# = 2.0$), set up to achieve a resolution similar to that the shadowgraph experiments ($239\mu m/pixel$). In order to keep laser light that reflected off the gas-liquid interface from interfering with the data acquisition, red fluorescent particles (Duke Scientific 36-5B, $24\mu m$ diameter) were used in conjunction with a red bandpass filter on the camera. This ensured that only light emitted by the particles

would reach the camera's CMOS sensor. The same jet speeds and nozzle diameters tested in the shadowgraph experiments were repeated during the PIV experiments, as shown in Table 1.3. For each condition, one 9-second PIV test was performed at a sampling rate of $1000Hz$.

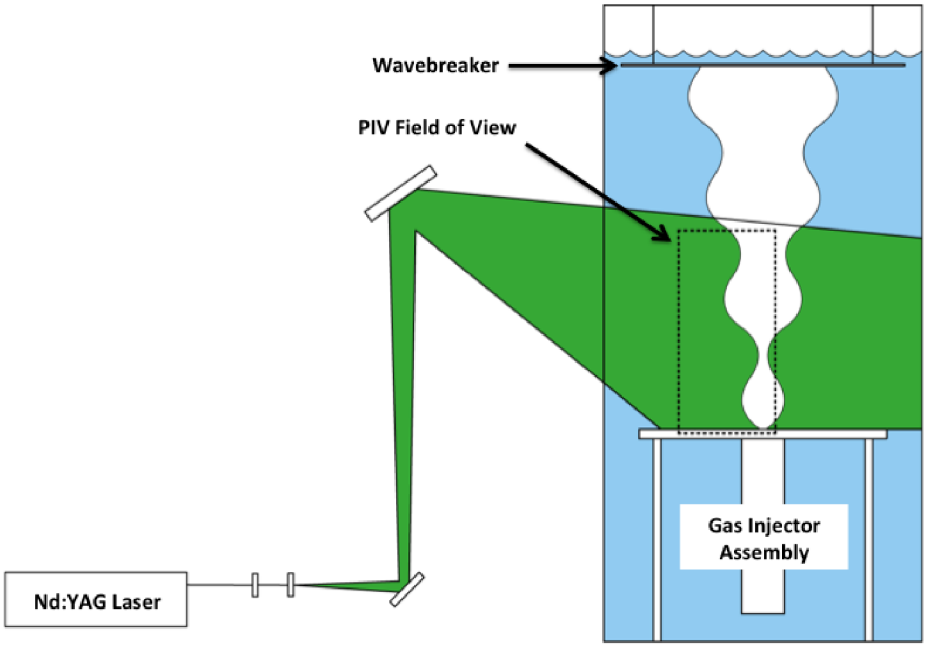

Figure 1.5: Schematic of the PIV experimental setup.

Table 1.3: PIV test matrix showing the measured Mach numbers

Design Speed	$d_0 = 3.175mm$	$d_0 = 6.35mm$
Mach 0.4	0.4438	0.3966
Mach 0.6	0.6381	0.6069
Mach 0.8	0.8581	0.8124
Mach 1.0	1.0110	1.0196
Mach 1.2	1.2199	1.3406
Mach 1.5	1.6079	1.6737
Mach 1.7	1.8829	1.8603
Mach 2.0	2.1240	2.1193

The experimental images were processed using a multiframe Robust Phase Correlation PIV algorithm. The Robust Phase Correlation (RPC) amplifies the signal-to-noise ratio of the PIV cross-correlation to produce velocity estimations that are accurate and robust to a variety of image conditions [14, 2, 15]. A multiframe algorithm is useful in experiments where a wide range of velocities is present, because relative error can become high in regions of the flow field where very low displacements occur due to high uncertainties in the small displacement estimations. The multiframe algorithm employed in this analysis skips intermediate image pairs in order to create a longer interframe time in low-displacement regions while preserving central difference-style velocity estimation. This increases the apparent displacement between the frames being correlated, resulting in a lower relative error. The quality criterion proposed by Persoons [16] was used to select the optimal interframe time. A qualitative comparison between data processed using a standard RPC algorithm and the multiframe algorithm showed that the multiframe processing produced vectors more uniform in both magnitude and direction.

The final PIV processing consisted of a two-pass multiframe algorithm that incorporated data with interframe times up to $5ms$. The first pass used an effective window resolution of 64x64 pixels with 50% overlap. The mean image window intensity was subtracted from each window to mitigate any effects of irregular particle illumination between frames. The resulting velocity field was validated using a two-pass universal outlier detection (UOD) method, as described in [17]. The second PIV processing pass used 32x32 pixel mean-subtracted windows with 75% overlap, followed by UOD validation.

Proper Orthogonal Decomposition

Proper orthogonal decomposition (POD), also known as Karhunen-Loéve decomposition, is a mathematical tool often used for the analysis of experimental or simulated flow fields [18]. It decomposes the time-varying velocity data into a sequence of modes that can be used to reconstruct a lower-order model model of the field. It approximates the velocity function, $u(x, y, t)$ as a finite sum:

$$u(x, y, t) = \sum_{n=1}^{N} a_n(t)\, \phi_n(x, y) \tag{1.8}$$

where $\phi_n(x, y)$ is an eigenmode, and $a_n(t)$ is the temporal projection coefficient. In the present work, POD was used to identify dominant flow structures in the PIV data and analyze their evolution throughout the flow regime studied.

1.3.2 Gas Properties

The variation of gas density and velocity with axial distance were not measured experimentally, but are required inputs for the Epstein model. However, the initial properties of the jet were recorded throughout each test, and the variation in cross-sectional area with axial distance could be determined from the radial position of the interface (assuming axisymmetric flow). From this data, isentropic relations can be used to describe the gas properties, as long as it can be assumed that the gas undergoes an adiabatic and reversible expansion between the nozzle and the free surface.

Since the jet is properly expanded at the exit plane, there should be no expansions or contractions that would result in a significant amount of heat transfer with the environment (neglecting the $0.04atm$ decrease in hydrostatic pressure over the $0.46m$ from the nozzle to the water surface). Thus, it can reasonably be assumed that the jet undergoes an adiabatic process.

Irreversibilities will occur in any flow, but previous studies seem to indicate that their effects are negligible in the case of a gas jet interacting with a liquid environment. Weimer et al. propose a model to predict how far a vapor jet will penetrate into a liquid bath that assumes isentropic behavior of the vapor [7]. The model matches well with their experimental penetration distances. Loth used isentropic relations in a model to predict the density and temperature distribution of an underwater gas jet, which matched reasonably well with experimental results [19]. Additionally, Epstein et al. found "near-isentropic" gas properties for a gas jet blown over a flat liquid surface [11]. Based on the results of these previous studies, it is assumed that isentropic relations will provide a sufficient estimation of the gas velocity and density in this study.

1.3.3 Theoretical Entrainment Coefficient

The entrainment rates presented by Epstein et al. are given in flow per unit area. Integrating around the circumference of the interface (assuming an axisymmetric jet) will result in predictions of the rate of change of the jet flow rate with axial distance. Proper nondimensionalization will produce an entrainment coefficient of the form proposed by Ricou-Spalding in Equation 1.3:

$$C_2 = \frac{d_0}{\dot{m}_0}\sqrt{\frac{\rho_g}{\rho_f}}\int_0^{2\pi} \dot{m}''_{ent} r\left(y\right) d\theta \tag{1.9}$$

$$= 2\pi r\left(y\right)\frac{d_0}{\dot{m}_0}\sqrt{\frac{\rho_g}{\rho_f}}\dot{m}''_{ent} \tag{1.10}$$

Here, r and θ are the polar coordinates of a point located along the circumference of the gas jet. Plugging in Equations 1.4, 1.6, and 1.7 results in expressions for the entrainment coefficient using the full Epstein model, as well as the RT and KH asymptotic solutions, respectively:

$$C_{2,full} = \frac{2\pi}{\sqrt{3}}\frac{d_0}{\dot{m}_0}\rho_g v\left(y\right) r\left(y\right)\sqrt{\frac{6\Psi}{1+\left(1+3\Psi\right)^{1/2}}+1} \tag{1.11}$$

$$C_{2,RT} = 2\pi\frac{d_0}{\dot{m}_0} r\left(y\right)\sqrt{\frac{2}{3}\rho_g\left(3\sigma\rho_f a\left(y\right)\right)^{1/2}} \tag{1.12}$$

$$C_{2,KH} = \frac{2\pi}{\sqrt{3}}\frac{d_0}{\dot{m}_0}\rho_g v\left(y\right) r\left(y\right) \tag{1.13}$$

Rather than a constant, as proposed by Ricou-Spalding, the Epstein model predicts that the entrainment coefficient will vary nonlinearly as the gas properties and interfacial dynamics evolve with axial distance from the nozzle.

1.4 Experimental Results and Discussion

1.4.1 Jet Dynamics

Quantifying the dynamics of the gas-liquid interface was required in order to determine the jet radius and interfacial acceleration for the Epstein model. Raw data from the shadow-

graph edge detection algorithm was processed using a temporal low-pass filter to eliminate high-frequency noise caused by random variations in the edge detection results between frames. This filtered boundary position was numerically differentiated with respect to time to determine interfacial velocity and acceleration normal to the axis of the jet. The largest instantaneous accelerations tend to occur as flow near the measurement location takes on a more bubbly character, while jetting flow is characterized by lower instantaneous accelerations.

The Root Mean Square (RMS) of the acceleration time history was computed to estimate $a\,(y)$ in the Epstein model. The RMS was computed over the five shadowgraph tests for each case; neglecting the first one second of data and any portion of the gas jet not attached to the nozzle. Figure 1.6 shows the RMS accelerations plotted against axial distance from the nozzle for the two exit diameters tested. The curves show a maximum near the nozzle, and tend to decrease with increasing axial distance. It is also noted that lower jet speeds generally exhibit higher RMS accelerations, as do the $6.35mm$ nozzles compared to the $3.175mm$ nozzles. This indicates that the RT instability may play a more dominant role in the entrainment process for larger jets, and as the flow transitions from a jet to a bubbly plume.

The jet radius, $r\,(y)$, was taken to be the average of the radial position over the five shadowgraph tests for each set of initial conditions. In the case of pinch-off events, only the orifice-attached portion of the jet was analyzed. As in the RMS acceleration calculations, the first one second (500 frames) of data was neglected to ensure that the jet had reached a steady-state condition. The results of this computation are presented in Figure 1.7. While some of the higher jet speeds spread more than some of the slower jets, the curves appear relatively independent of jet speed. They show a linear trend at axial distances greater than approximately 5 diameters. However, near the nozzle, rather than approaching a radius of $0.5d_0$ as would be expected, the mean boundary balloons outward to as high as $6d_0$. This trend is especially prevalent at the low jet speeds, although even the boundary of the Mach 2.1 jets remains greater than $1.0d_0$ near the nozzle. This reason for this is illustrated in Figure 1.8 by looking at the shape of the jets at two different time instances. The jet boundary approaches $0.5d_0$ in frames (a) and (c). However, frames (b) and (d) show a difference in the near-orifice boundary position, where the jet balloons out significantly. This effect,

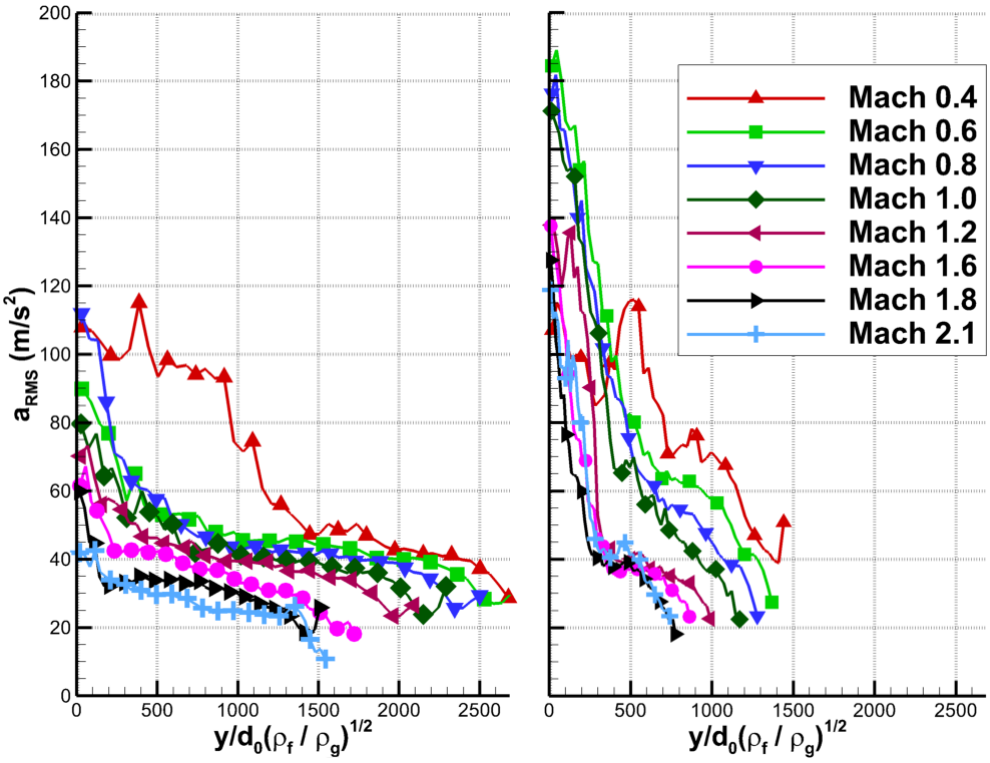

Figure 1.6: RMS interfacial acceleration plotted against axial distance from the nozzle for the 3.175mm exit diameter (left) and the 6.35mm exit diameter (right).

while more pronounced at low jet speeds, is seen across the entire range of Mach numbers (although only the two extremes are presented in Figure 1.8 for brevity).

This ballooning near the nozzle brings into question the validity of using one-dimensional isentropic relations to describe the gas density and velocity. Figure 1.9 presents the isentropic gas velocity alongside velocities computed using the empirical model developed by Tross [8], and the maximum bubble rise velocity of approximately $30 cm/s$ found by Talaia in [20]. All three velocity curves are characterized by a significant decay from the nozzle exit velocity even at very small axial distances, and approach the bubble terminal velocity far from the nozzle. Such a steep initial decline can be explained given the large variation in density (three orders of magnitude) between the liquid and gas. This results in the momentum of the gas jet, even at high initial velocities, being relatively small compared to the momentum required to accelerate the ambient liquid.

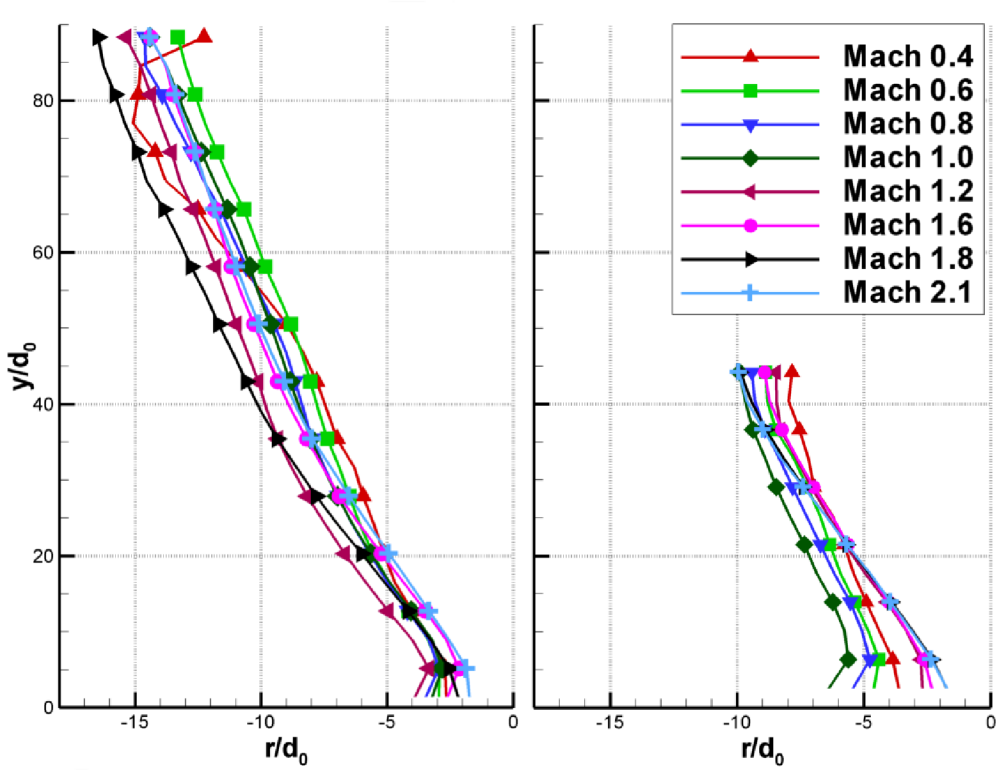

Figure 1.7: Mean interface boundary plotted against axial distance from the nozzle for the 3.175mm exit diameter (left) and the 6.35mm exit diameter (right).

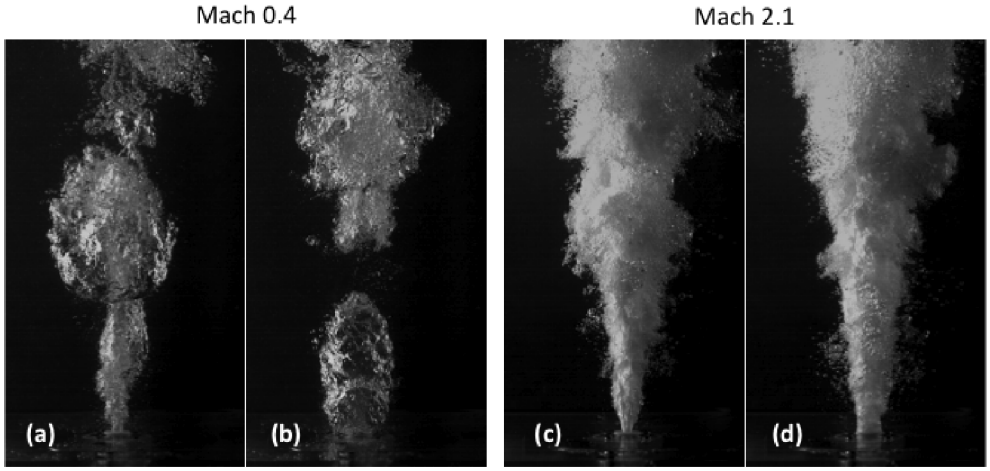

Figure 1.8: Sample shadowgraph images from the 6.35mm exit diameter Mach 0.4 tests (left) and Mach 2.1 tests (right).

The Tross model was evaluated both at the jet centerline and the mean jet boundary (obtained from the shadowgraph experiments). Note that this model predicts the mean bulk velocity, making no distinction between the gas and liquid phases. However, a significant slip velocity between the two phases was found by Ito et al. in [21]. This may account for much of the velocity reduction moving from the centerline to the mean boundary, and explains why the gas velocity computed at the boundary dips below the bubble terminal velocity at low jet speeds. The isentropic velocity is very close to the Tross model at high jet speeds, which lends credence to the isentropic assumption made in this and other studies (see Section 1.3.2). At low jets speeds, the isentropic velocities are higher than the Tross model predicts. However, these jets are characterized by a high number of pinch-off events where liquid penetrates to the jet centerline. Since the high-density liquid moves significantly slower than the low-density gas, a lower mean bulk velocity is to be expected. The actual gas velocity is likely to be closer to the isentropic curve (as in the high-velocity jets) if proper exception were made for the reduction in bulk velocity caused by pinch-off events.

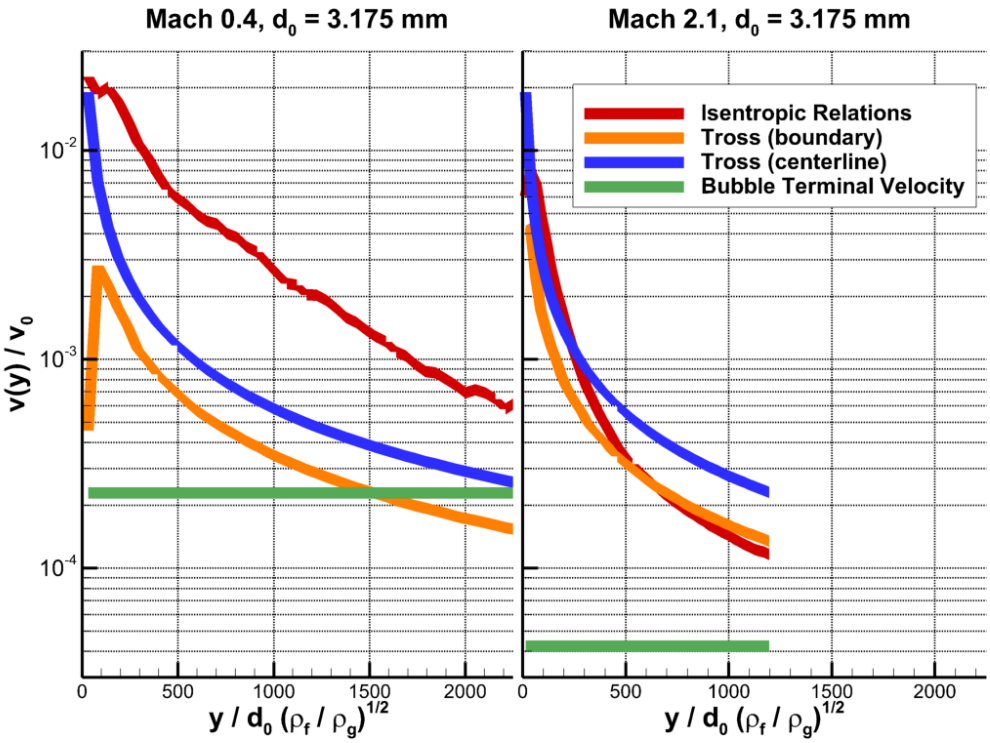

Figure 1.9: Gas velocity models as a function of axial distance from the nozzle for the $d_0 = 3.175mm$ tests (left) and $d_0 = 6.35mm$ tests (right).

1.4.2 Flow in the Ambient Fluid

A sample of the PIV results with vectors showing the flow direction and the background contour representing the velocity magnitude is presented in Figure 1.10. The domain occupied by the gaseous phase was detected in each frame of the PIV data using the correlation strength of each vector in the flowfield. In cross-correlation based PIV algorithms, such as the RPC method used in this experiment, displacement is estimated from the location of the highest peak in the correlation matrix. The correlation strength was estimated using the amplitude of this peak, which has been found to decrease at weak signal-to-noise ratios (SNR's) [22], using the logic that the areas of the image where the gas jet exists should have a low SNR because there are no particles to correlate. A correlation strength threshold was first applied, followed by a dilation and erosion of the regions with low correlation in order to form a continuous area representing the gaseous phase. As seen in Figure 1.10, the masking algorithm performed well in detecting regions of the flow field occupied by the jet.

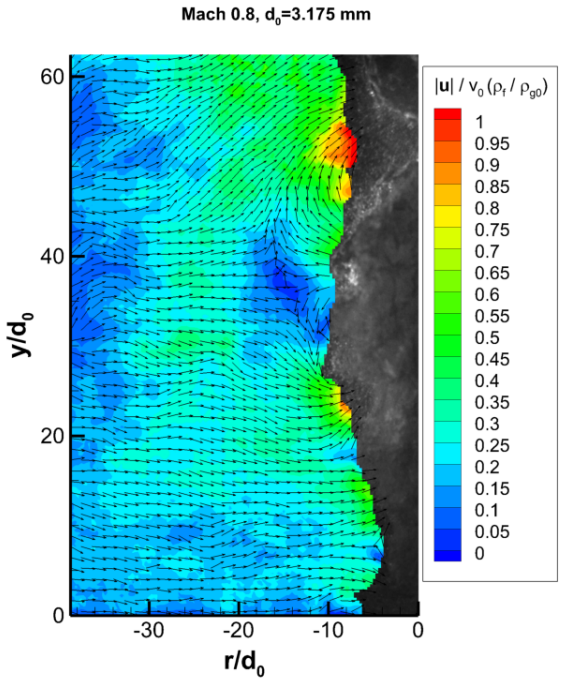

Figure 1.10: Sample PIV velocity field from a $d_0 = 3.175mm$, Mach 0.8 test.

In the Ricou-Spalding model, the initial mass flow rate of the gas jet is used to normalize the total mass flow rate as a function of axial distance. This implies that the momentum

of entrainment in the fluid should scale with the initial jet momentum for a common nozzle diameter. This leads to a nondimensionalization of the fluid velocities, **u**:

$$\frac{\mathbf{u}}{v_0}\frac{\rho_f}{\rho_{g0}} \tag{1.14}$$

Figure 1.11 shows the mean velocity fields for a representative sample of the $d_0 = 3.175mm$ test cases, normalized using Equation 1.14. Rather than remaining constant across the range of initial jet velocities, the normalized entrainment momentum drops with increasing jet speed. In order to quantify this, a common-base POD processing [23] was performed by concatenating the normalized velocity data from consecutive jet speeds into two large data sets; one for each nozzle diameter. This allowed for a baseline comparison of the results across the range of jet speeds studied.

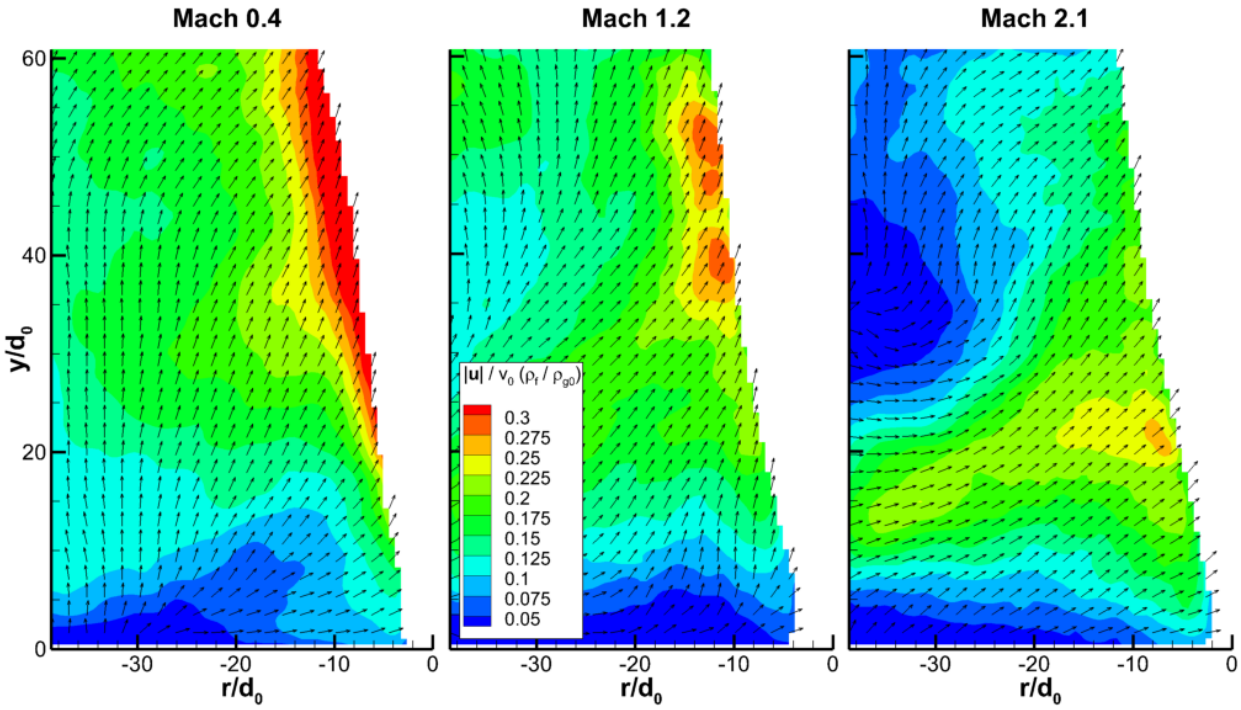

Figure 1.11: Mean velocity fields for a representative sample of the $d_0 = 3.175mm$ test cases, normalized using Equation 1.14.

The 0^{th}-order mode simply contains the mean velocity information, since the mean was not subtracted from the data prior to performing the POD. The time-average of the 0^{th}-order

projection coefficient over the length of each test is plotted in Figure 1.12. This quantifies the average energy contained in the 0^{th}-order mode as a function of jet speed. As was shown qualitatively in Figure 1.11, the mean normalized entrainment velocity drops with increasing jet speed, rather than remaining constant as predicted by the Ricou-Spalding model. However, above Mach 1, the curve levels out to what appears to be an asymptotic solution on the order of 10^{-1}. This suggests that the subsonic jets, characterized by significant bubbling, will have higher entrainment rates than the supersonic jets, but that entrainment may scale with increasing jet speed (as predicted by Ricou-Spalding) in the jetting regime.

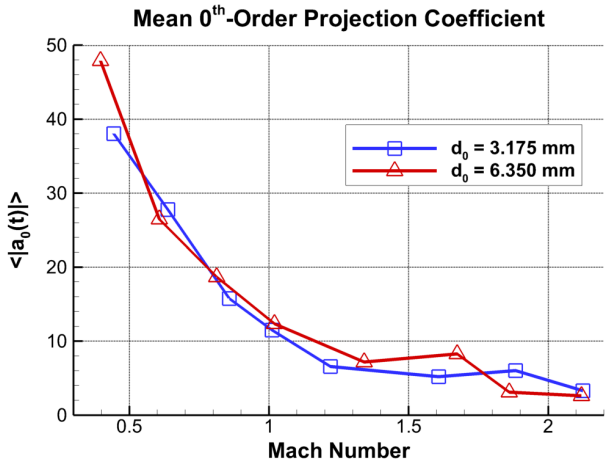

Figure 1.12: Mean projection coefficient from the POD performed on the normalized PIV flow fields, plotted against jet speed.

The fluctuating modes are characterized by vortical structures, as seen in Figure 1.13. These plots are contoured by nondimensionalized vorticity, computed by multiplying each mode by its mean projection coefficient, taking the spatial derivatives, and normalizing by the nozzle diameter. The first two modes suggest the presence of two distinct pinch-off locations, while the third contains a large region that pushes flow away from the jet except at a small region near the pinch-off location seen in the first mode. Figure 1.14 shows the phase portrait between the first- and second-order projection coefficients. The circular shape of the phase portraits indicates an oscillation between the two modes, which would occur as disturbances on the jet interface pass through the flowfield, producing vortices in the flow field that augment the mean entrainment flow.

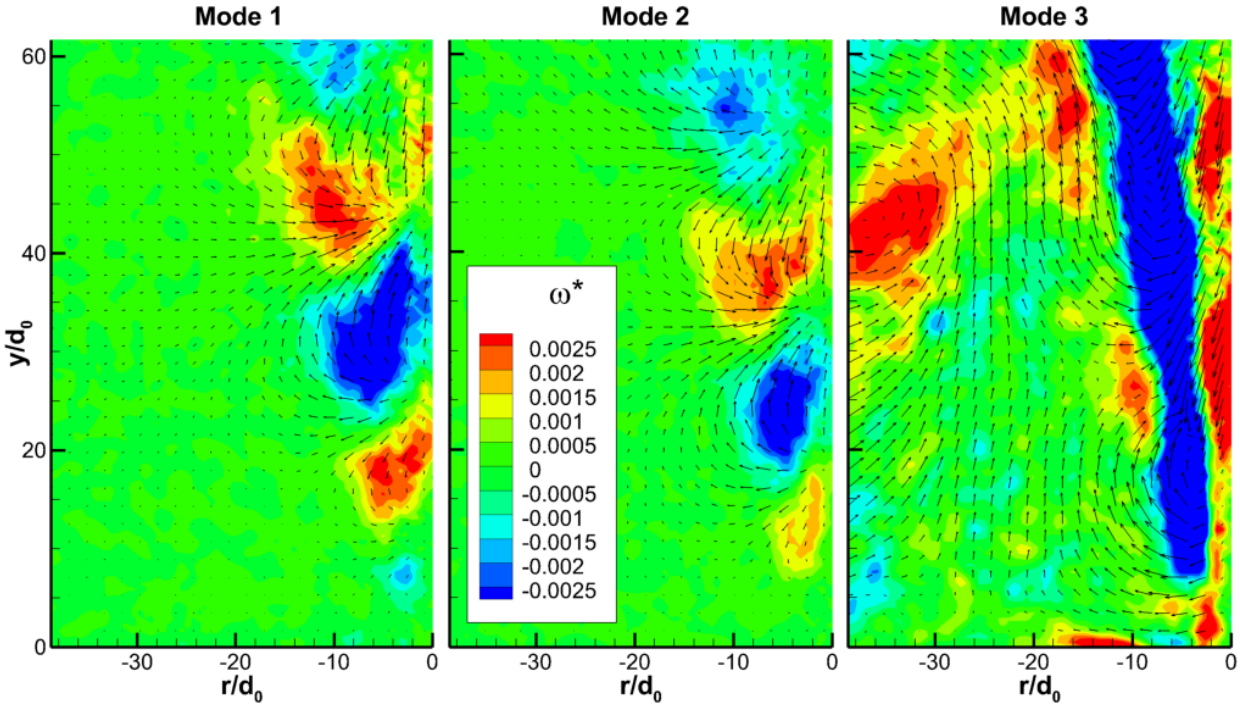

Figure 1.13: The three most dominant fluctuating modes from the $d_0 = 3.175mm$ POD results, contoured by vorticity.

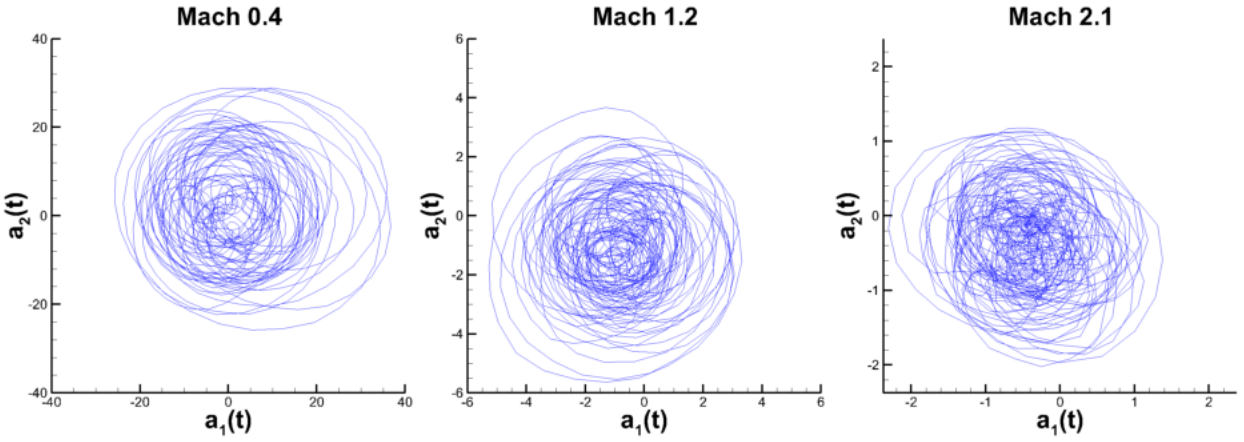

Figure 1.14: Phase portrait between the projection coefficients of the first and second order for a representative sample of the $d_0 = 3.175mm$ jets.

The power spectra of the projection coefficients was computed in order to analyze the propagation speed of structures in the flow across the range of jet speeds studied. As the jet speed increases, the peak in the power spectra shifts towards higher frequencies. The Strouhal number for each jet was computed using the location of this peak, f_{peak}, as the characteristic frequency, the nozzle diameter as the characteristic length scale, and the initial gas velocity as the characteristic velocity:

$$St = \frac{f_{peak} d_0}{v_0} \tag{1.15}$$

The results of this calculation are presented in Figure 1.15. Although the peak frequency increases with jet speed, the higher gas velocities still result in smaller Strouhal numbers than in the low-speed jets. This indicates that the characteristic velocity of the interfacially-driven flow structures does not scale with jet speed in the subsonic jets, suggesting an increasing slip velocity in the gas jet at high gas velocities. However, as seen in the mean project coefficient, the Strouhal number appears to approach an asymptotic solution in the supersonic jets, indicating that the frequency of oscillation of the flow structures scales with the initial gas velocity.

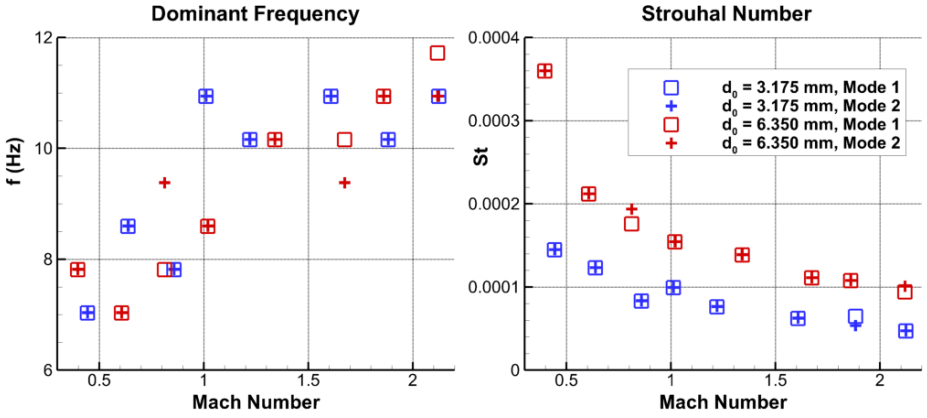

Figure 1.15: Strouhal number calculated using the peak frequency in the POD projection coefficients' power spectra, nozzle diameter, and initial jet speed normalized by density ratio; plotted against jet speed for the first and second POD modes.

Entrainment was quantified using a novel control volume (CV) approach, by assuming a conservation of mass in the volume. The mass flow entering a CV at each time instant was assumed to have become entrained into the jet. A sample flowfield with a representative

control volume is shown in Figure 1.16. Multiple rectangular CV's with varying heights were applied to the mean PIV fields to obtain entrainment as a function of axial position. The top of the CV was always placed at the mean interface at each measurement location.

The results of this entrainment computation are presented in Figure 1.17. The total jet flow rate, equal to the sum of the initial gas flow and the entrained liquid mass, is nondimensionalized by the initial flow rate. This is plotted against a nondimensionalized axial distance that incorporates the density ratio. Ricou-Spalding's linear relationship is plotted for comparison. The model matches reasonably well with the high speed jet results near the nozzle. However, the experimental curves take on an exponential shape as axial distance increases, rather than the linear shape predicted by Equation 1.1. This may be a result of increased advective entrainment, not accounted for in the model, as the jet begins to pinch off.

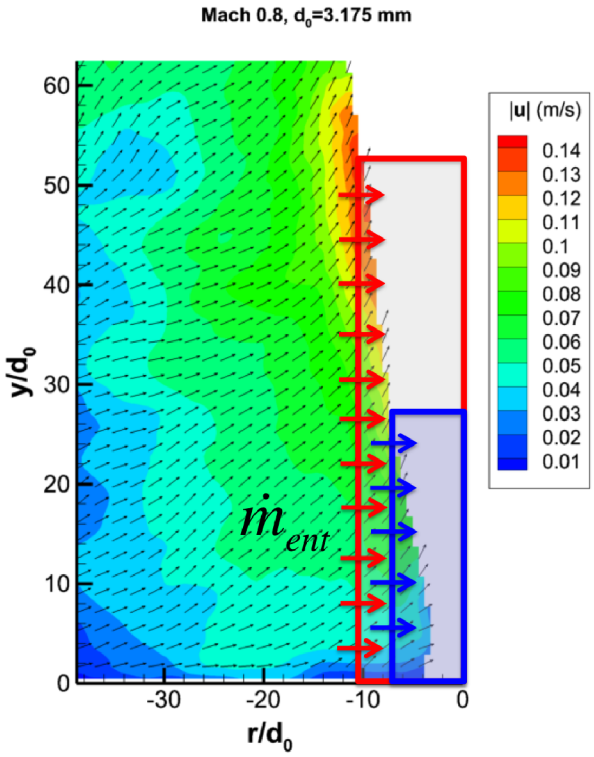

Figure 1.16: Mean velocity field for the $d_0 = 3.175mm$ Mach 0.8 jet illustrating the control volume method used to quantify entrainment.

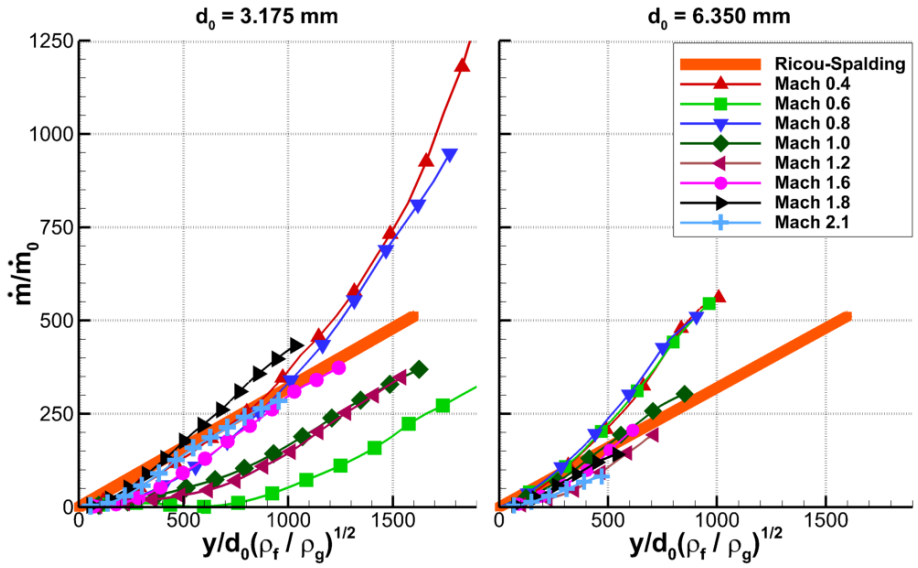

Figure 1.17: Total jet flow rate as a function of axial distance for the 3.175mm jets (left) and the 6.35mm jets (right).

1.4.3 Relative Importance of the RT and KH instabilities

To determine the relative importance of RT and KH instabilities, Ψ was computed using constants for the surface tension and fluid density ($\sigma = 0.72N/m$, $\rho_f = 1000kg/m^3$), the isentropic gas density and velocity, and the RMS acceleration results from the shadowgraph experiments. The results, presented in Figure 1.18, show values of Ψ ranging from 10^{-2} to 10^7. The curves show a minimum close to the nozzle, and increase significantly with axial distance. This minimum is greater than 100 for subsonic tests but decreases with increasing jet speed, suggesting that the KH instability will play a larger role in entrainment at supersonic jet speeds, especially at low axial distances. Further away from the nozzle, the RT instability is likely to dominate.

The entrainment coefficient predicted by the Epstein model is presented in Figure 1.19, along with the experimental data and the Ricou-Spalding model. Plotted for comparison are asymptotic solutions to Epstein's model. In all cases, the curve for the full Epstein model is similar to that of the RT asymptote, indicating that the influence of the KH instability is small compared to that of the RT. The Epstein model shows worse agreement than Ricou-Spalding in most cases, exhibiting a tendency to overestimate the entrainment

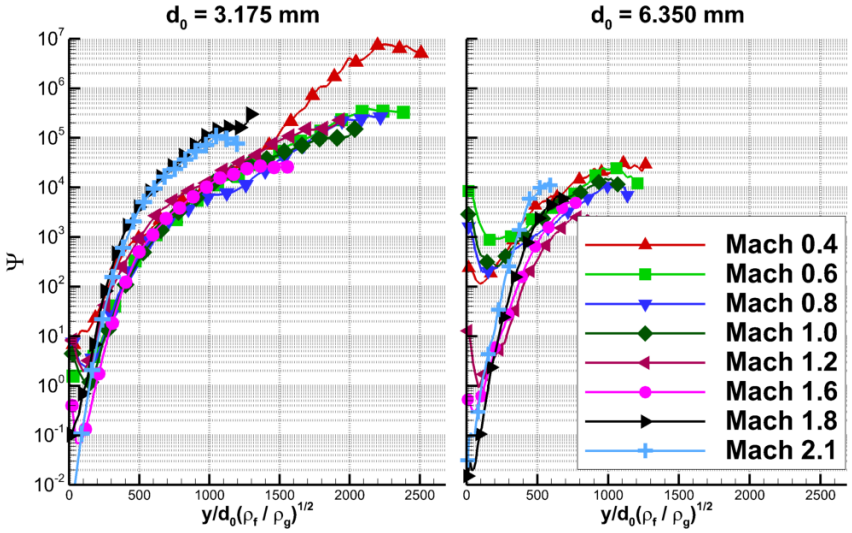

Figure 1.18: Total jet flow rate as a function of axial distance for the 3.175mm jets (left) and the 6.35mm jets (right).

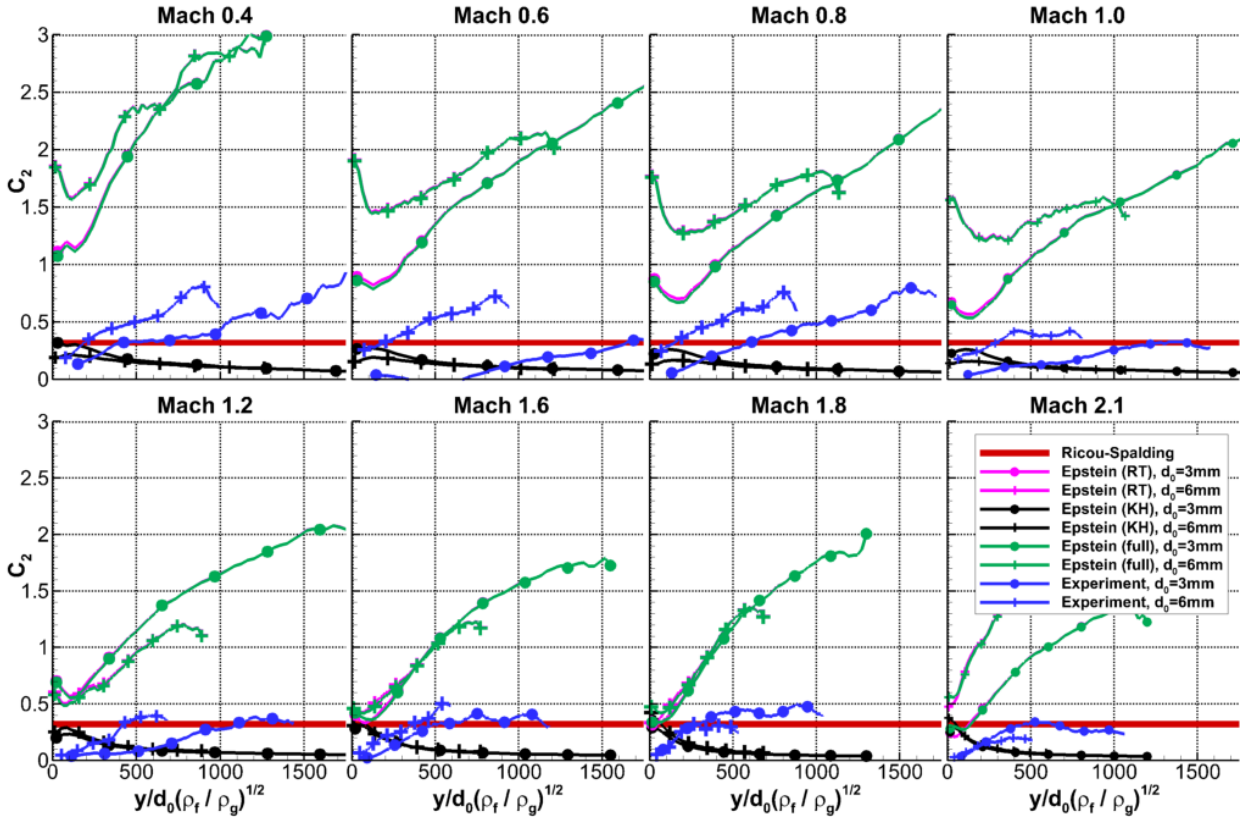

Figure 1.19: Entrainment coefficient, C_2, plotted against nondimensionalized axial distance from the nozzle.

rate significantly. The Epstein model does, however, predict the increase of the entrainment coefficient with axial distance seen in the experimental results. This increase may be caused by higher advective entrainment, especially at lower jet speeds or high axial distances, as Ψ becomes larger.

1.4.4 Limitations of the entrainment models examined

Neither entrainment model predicted the experimental results satisfactorily. In the case of the Ricou-Spalding model, the entrainment momentum was found to not scale linearly with jet momentum at low jet speeds. This is likely due to interfacial effects and bubbling producing additional advective entrainment that cannot be accounted for in a model developed for single-phase flows. The Epstein model's tendency to greatly overestimate entrainment may be a result of (1) wave growth different from that predicted, or (2) a poor assumption relating wave growth to entrainment. In the case of (1), the model assumes an incompressible semi-infinite domain. This is characteristically different from a radially-confined domain with a compressible gas. The confined domain may restrict the growth of interfacial waves, resulting in less entrainment. In (2), Epstein assumed that droplets breaking off from the interface would have a diameter on the order of half the most energetic wave's wavelength. Smaller droplets would result in less entrainment than predicted, even if wave growth is modeled properly.

1.5 Conclusions

Entrainment by underwater gas jets was studied using a combination of shadowgraph and PIV experiments. From the results of these experiments, it can be concluded that:

1. Entrainment by underwater gas jets is due to a combination of interfacial instabilities. This is contrary to previous research on multi-phase flows, where an assumption is often made that the KH instability will dominate and the RT instability is neglected.

2. Entrainment models developed for single-phase flow are inadequate in predicting entrainment in two-phase jets.

3. The two-phase entrainment model examined in this study tended to over-estimate entrainment rates obtained from the PIV data, but predicts the increase in the rate of entrainment with axial distance from the jet nozzle seen in the experimental results.

Chapter 2

Spectral Phase Correlation for Particle Image Velocimetry

2.1 Introduction

The phase correlation method is traditionally used to measure image shifts in MRI data and aerial imagery [24], but has been largely overlooked as a PIV processing method (with the exception of a preliminary study which showed poor results [25]). The phase correlation method is based on the Fourier Shift Theorem, which implies that signal displacements between two successive images (I_1 and I_2) are proportional to a phase shift in the spectral domain:

$$I_2(k) = I_1(k)\, e^{-jk\tau} \tag{2.1}$$

where k is the wavenumber based on digital frequency, and τ is the time delay between the two images. The phase shift is estimated from the phase correlation matrix, Ω:

$$e^{-jk\tau} \approx \Omega(k) = \frac{I_2(k)\, I_1^*(k)}{|I_2(k)\, I_1^*(k)|} \tag{2.2}$$

where * denotes a complex conjugate operation. The image shift can then be directly measured by estimating the resultant linear slope of the phase with respect to wavenumber.

Current cross correlation (CC)-based PIV processing algorithms (the yellow and blue paths in Figure 2.1) transform this phase information back to the spatial domain and determine particle displacement based on the location of the dominant peak. The Spectral Phase Correlation (SPC) (the magenta path in Figure 2.1) however, computes displacement directly in the Fourier domain. This has multiple advantages over existing CC-based methods, and represents a new paradigm in PIV processing. The displacement vector is estimated by unwrapping the aliased phase correlation matrix and determining the orientation of the resulting plane. This eliminates errors introduced by peak detection algorithms, which tend to select integer-valued displacements. Additionally, the phase information is decomposed into modes using singular value decomposition (SVD). This modal analysis provides information about the quality of the correlation, as well as about additional flow features and background noise in the image windows.

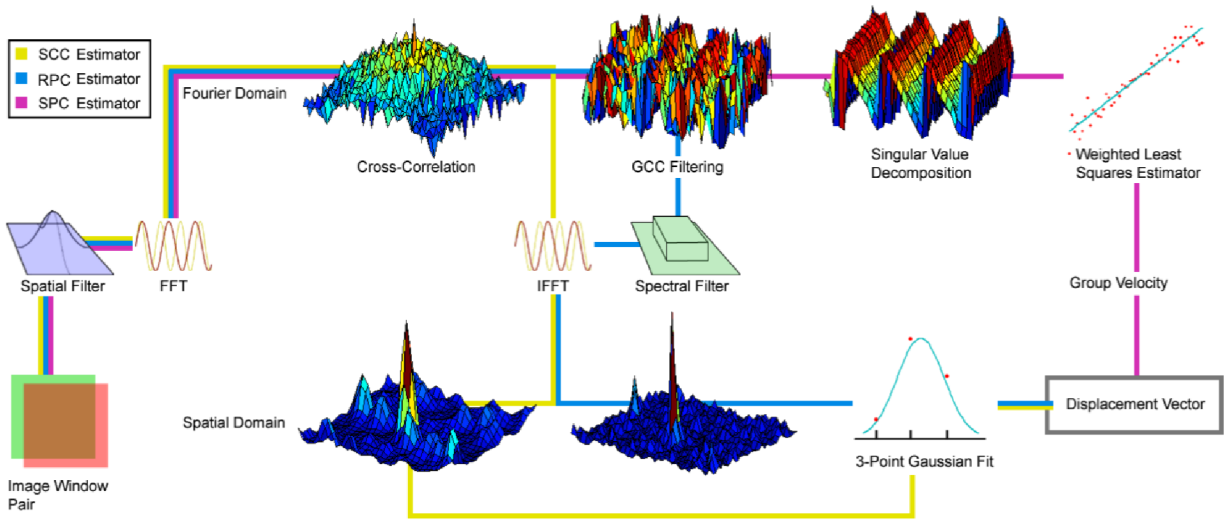

Figure 2.1: Flow chart depicting current CC-based and Spectral Phase Correlation PIV processing algorithms. [2]

In this work, a significant improvement in the SPC processing method will be demonstrated through the application of filtered image windows and an analytically derived weighting function that estimates the signal-to-noise ratio (SNR) of each frequency component. It is then shown how the SPC approach supplements or improves on existing ensemble, multiframe, and adaptive windowing techniques by allowing for phase information from multiple correlations to be scaled and overlaid when performing the weighted least squares regression to determine the slope of the correlation plane. Using this method allows information from

windows with multiple interframe times and window sizes to be incorporated into a single displacement estimation. Additionally, limitations in the current SPC algorithm will be addressed, and suggestions for further improvement will be offered.

2.2 Spectral Phase Correlation

2.2.1 Implementation

The general SPC algorithm is illustrated in Figure 2.1, and expanded upon here:

1. A Gaussian filter is applied to the image window pairs to help eliminate wrap-around aliasing [15].
2. A Fourier-based cross-correlation is performed on the filtered windows, and the phase correlation matrix is computed using Equation 2.2.
3. A singular value decomposition (SVD) decomposes the phase correlation matrix into u- and v-modes.
4. The phase angle of the dominant mode in each direction is "unwrapped" from a saw-tooth pattern to form a line of scattered data.
5. A weighted least squares (WLSQ) regression is used to determine the slope of the data, from which displacement is determined.

CC-based algorithms follow a similar process, but deviate at step 3, where they instead perform an inverse Fourier transform. This produces a peak in the spatial domain from which displacement is determined.

The SVD decomposes the noisy phase correlation matrix into u- and v-modes. It produces a factorization of the form:

$$\Omega = U\Sigma V^* \tag{2.3}$$

where U and V are matrices whose columns contain the modes of the v- and u-velocity components, respectively, and Σ is a diagonal matrix of "singular values," equal to the

square root of the eigenvalues of $\Omega\Omega^*$. Thus, the SVD decomposes the cross correlation into two sets of vector modes (vertical and horizontal), as well as an eigenvalue-based measure of how significantly each contributes to the total signal.

As seen in Figure 2.2, the phase correlation matrix is bounded between $\pm\pi$. This causes the dominant modes isolated using the SVD to be aliased, resulting in a characteristic sawtooth pattern. In the present implementation, these discontinuities are located using a threshold of π, and are unwrapped to form the phase vector; the slope of which provides information about displacement. The high-frequency tails of the unwrapped phase vector are contaminated by noise, which would introduce significant error into calculation of the vector's slope. To remedy this, a previously derived model based on the theoretical SNR is applied to the unwrapped phase vector during the weighted least squares regression:

$$W_k = \begin{cases} exp\left(\frac{-d_e^2 k^2}{16}\right) & |k| \leq \frac{2}{\pi d_e} \\ 0 & |k| > \frac{2}{\pi d_e} \end{cases} \quad for \quad -\pi \leq k < \pi \tag{2.4}$$

where d_e is the effective particle image diameter. This model was developed as a spectral filter for the Robust Phase Correlation (RPC), a CC-based algorithm, which provides substantial reductions in bias errors over other processing algorithms [2]. The form presented in Equation 2.4 assumes that random errors are much greater in magnitude than errors due to aliasing of the phase information.

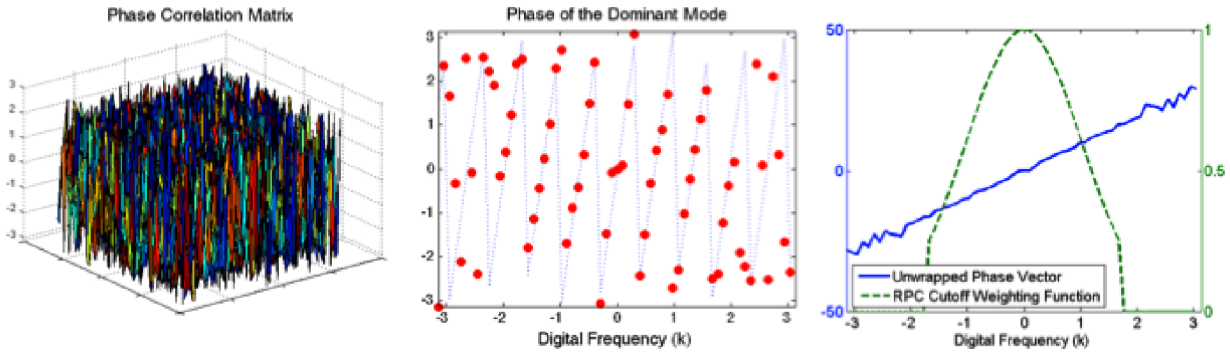

Figure 2.2: Phase Correlation Matrix (left), the phase of the dominant mode from the SVD (center), and the unwrapped phase with the RPC cutoff weighting function (right).

2.2.2 Monte Carlo Simulations: Uniform Flow

To quantify the effect of the RPC weighting function and test the performance of the SPC compared to existing CC-based methods, 8-bit artificial images of uniform flow with varying displacement and Gaussian white background noise levels were generated using Monte Carlo simulations. The particle images were assumed to follow a Gaussian profile with $\sigma = \sqrt{2} pixels$, and were randomly distributed with a density of $0.00977 particles/pix^2$. Perspective effects and out-of-plane motion between frames were not accounted for in the simulations. Displacements ranged from 0 to 25 pixels, and the zero-mean background noise level varied from 0% to 10%. The images were evaluated using unfiltered 32x32 pixel windows in the SCC algorithm, and 64x64 pixel Gaussian filtered windows with signal content equivalent to that of a 32x32 pixel window [15] in the RPC algorithm. The SPC method also used filtered windows with a 32x32 pixel equivalent size, but the data was first processed using unfiltered windows to quantify the effect of Gaussian filtering on the results. A single-pass processing with a grid size of 16x16 pixels resulted in 2016 sample windows per 2046x2046 pixel image. Statistical convergence was checked by examining the total error as a function of grid samples.

Since displacement remained constant throughout each image, a statistical error analysis was performed on the velocity measurements. Bias error, total error, and random error were defined, respectively, as:

$$e_{bias} = \frac{1}{n}\sum_{i=1}^{n}(u_i - u_{act,i}) \tag{2.5}$$

$$e_{total} = \sqrt{\frac{1}{n}\sum_{i=1}^{n}(u_i - u_{act,i})^2} \tag{2.6}$$

$$e_{random} = \sqrt{e_{total}^2 - e_{bias}^2} \tag{2.7}$$

where u_i is a velocity measurement and n is the number of measurements. These statistics were computed after removing outliers in the velocity field, defined as measurements with an absolute error greater than 0.5 pixels.

2.2.3 Results in Uniform Flow

The Gaussian window filtering and RPC weighting function employed in the novel SPC algorithm result in a significant improvement over simpler phase correlation methods. Figure 2.3 shows an error analysis of the SPC uniform flow data that quantifies the effect of these additions. The window filtering provides significant reductions in both bias and random error by eliminating wrap-around aliasing due to the periodic nature of the discrete Fourier transform [15]. However, significant "peak locking" (a tendency to select integer-valued displacements) still occurs in all the un-weighted data. This effect must be attributed to the high-frequency phase information that would be ignored or assigned a low weight by the RPC function, because including the weighting function essentially eliminates peak locking (except in the unrealistic case of 0% background noise).

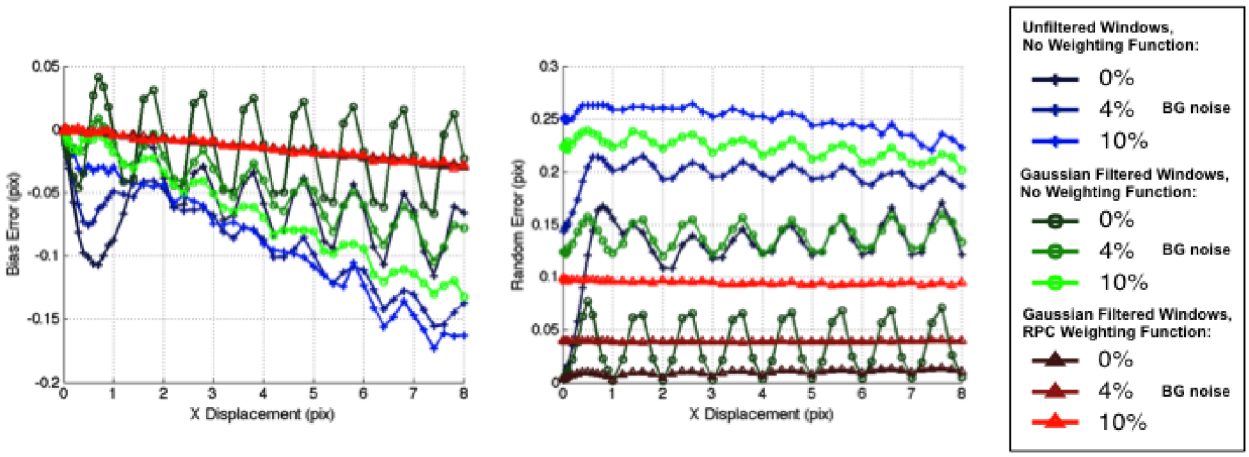

Figure 2.3: Error analysis of the SPC uniform flow data demonstrating the effect of Gaussian-filtered windows and the RPC weighting function.

As seen in Figure 2.4, the novel SPC algorithm incorporating Gaussian filtered windows and the RPC cutoff weighting function provides a significant decrease in both bias and random error over the SCC. The RPC produces a lower random error than the SPC, particularly at high noise levels. This is presumed to be an effect of increased noise levels in the phase correlation matrix causing poor unwrapping of the dominant modes. However, the SPC results with background noise do not exhibit the peak locking effect seen in the RPC curves.

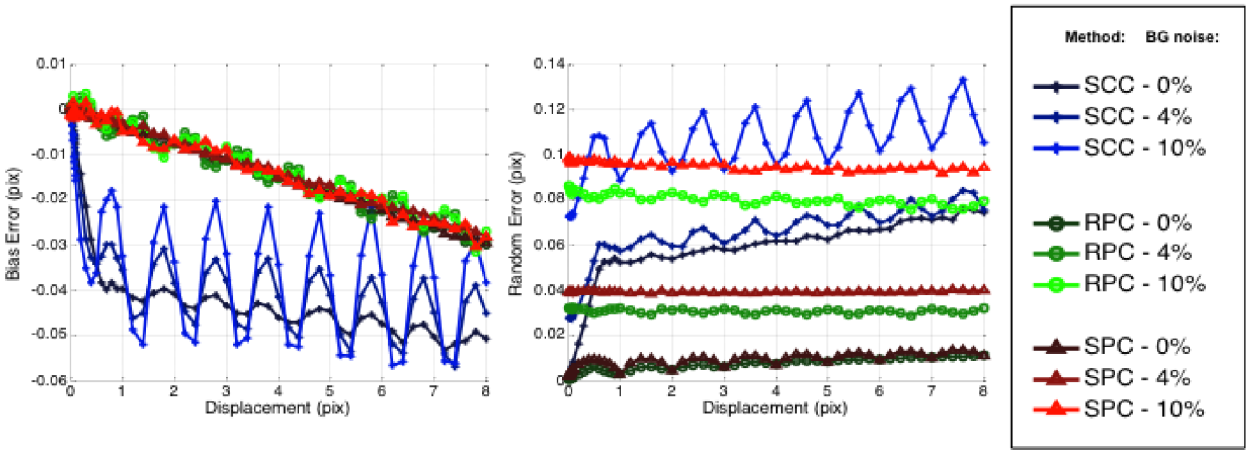

Figure 2.4: Error analysis of the uniform flow data comparing the SPC to CC-based processors.

The results presented in Figure 2.4 show that the performance of the SPC degrades with increasing background noise and displacement. One method of quantifying the quality of the phase correlation is to analyze the eigenvalues in the Σ matrix computed by the SVD. A high ratio between the first and second eigenvalues should be indicative of a strong signal being contained in the first mode, with a low amount of noise in the remaining modes. This is similar to the concept incorporated in some CC-based multiframe PIV algorithms [26, 16] of using the ratio between the height of the most significant and second-most significant peaks in the spatial domain to assess correlation quality. The eigenvalue ratio can then be used to assess the probability that a given measurement will correctly identify the proper slope in the phase vector, and therefore estimate the correct displacement.

The left panel of Figure 2.5 shows a plot of the percentage of vectors in synthetic uniform flow images (the generation and evaluation of which was discussed in Section 2.2.2) with an absolute error in the displacement estimation of greater than $0.5pix$ (Bad Vector Percentage, or BVP) against the ratio between the first and second eigenvalues. This ratio drops with increasing background noise, as well as with decreasing correlated particle image pairs (NF_iF_o, as defined in [22]) as seen in the right panel of Figure 2.5. For the tested cases, an eigenvalue ratio of better than 1.3-2.0 is required to guarantee that less than about 10% of the measured vectors results in an incorrect measurement, and ratios of about 1.5-2.3 for less than 1% failure rate. This is similar to results for the peak ratios of traditional CC approaches.

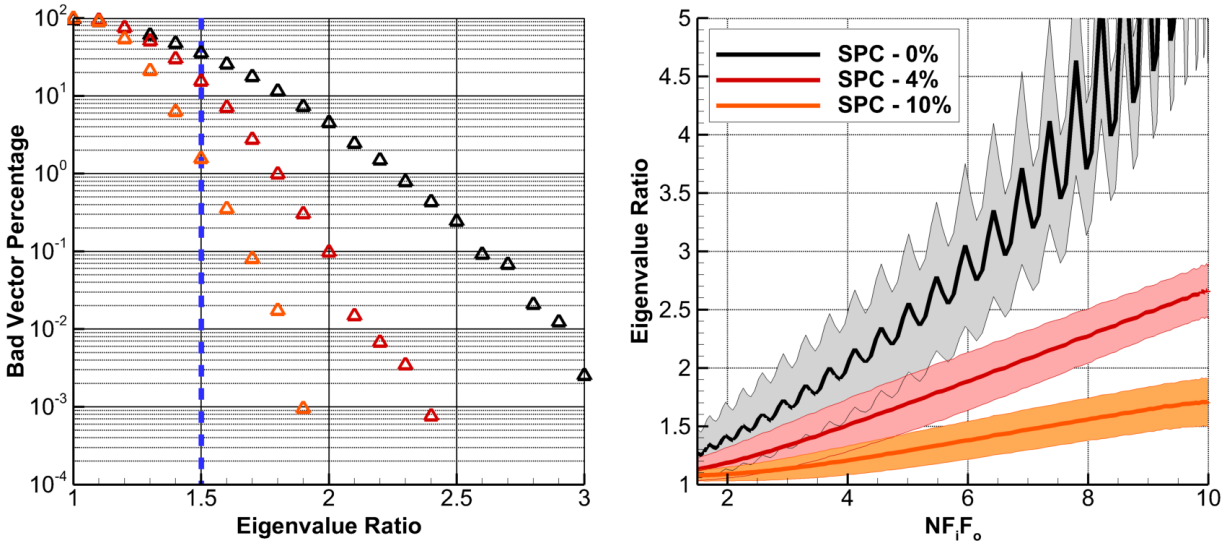

Figure 2.5: Bad vector percentage (BVP) plotted against eigenvalue ratio (left) and eigenvalue ratio platted against the number of correlated particle image pairs per window (right).

2.3 Ensemble Spectral Phase Correlation

Remaining in the frequency domain to perform the displacement estimation also suggests a straightforward method whereby information taken from correlation of image pairs can be simultaneously sampled to improve the accuracy of each measurement, even if the pairs have different interframe times or window sizes.

2.3.1 Background

The concept of using time-averaged correlations (ensemble PIV), multiple interframe times (multiframe PIV), or multiple window sizes (adaptive windowing) in the evaluation of PIV data has been explored before. Ensemble PIV is commonly used in applications with a low signal-to-noise ratio (SNR), such as micro-PIV (μPIV). In this technique, correlation planes in the spatial domain are computed for a number of subsequent image pairs. These correlation planes are then averaged together with the goal of recovering the actual signal, which may be obscured by random or uncorrelated noise in the instantaneous results. Ensemble averaging of the correlation planes has been found to significantly improve velocity

estimations on noisy data [27, 28], but is generally not used when the data has a high SNR because it requires the assumption of steady flow. This makes ensemble PIV unsuitable for experiments where unsteady information is needed, as in the computation of turbulent statistics or analysis of flow structures such as vortices.

Multiframe CC-based PIV algorithms have been developed by previous researchers [26, 29, 16] with the goal of increasing the velocity dynamic range (VDR) of PIV, defined as the ratio between the highest and lowest resolvable velocities. This is accomplished by dynamically adjusting the interframe time throughout the flow field to obtain optimal particle image shifts for the correlation algorithm. At short interframe times, relative error on the velocity estimations can become very high. However, if the interframe time is extended too much, effects such as high particle displacement, out-of-plane motion of the particles, and shearing or rotation of the window may decrease the SNR. Traditional multiframe algorithms correlate multiple frame pairs and attempt to optimize the interframe time. This additional computational expense is underutilized, however, as often only one frame pair is ultimately used in the velocity estimations, and at best several noisy displacement estimates are averaged together.

The goal of a multiframe PIV algorithm is to expand the range of velocities over that measured using a constant interframe time. Similarly, an adaptive windowing algorithm is used to enhance spatial resolution over that of an algorithm using a constant interrogation window size. Too small of a window, especially in flow regions with few particles, will result in loss of correlation. However, too large of a window will obscure finer features of the flow. Adaptive windowing algorithms such as that presented in [30] select an optimal window size for the seeding density of each window. This was found to reduce outliers in image regions with a low SNR while maintaining high spatial resolution in areas of high shear and rotation, and required less fine-tuning of the window size by the user than a standard PIV algorithm.

2.3.2 Implementation

Extending the novel SPC algorithm to an ensemble method that incorporates data from multiple correlations, possibly with multiple interframe times or window sizes, brings a unique set of challenges. Most CC-based multiframe or adaptive windowing algorithms se-

lect one interframe time or window size at a time, respectively, so they need only to determine which will produce the best correlation. When information from multiple frame pairs is used simultaneously, the problem in multiframe or multiwindow PIV is extended from selecting the optimal correlation to determining which correlations will improve the displacement estimation and which will detract from it. When done properly, combining correlation information before the measurement of displacement should offer improved accuracy over simply averaging the resultant velocities from each individual correlation by boosting the SNR of the correlation (similar to traditional ensemble PIV).

The term *particle image pair* (PIP) is used to refer to a pair of interrogation windows. The ensemble algorithm described here and illustrated in Figure 2.6 can be implemented using the following procedure as either a multiframe or multiwindow algorithm by varying the appropriate parameter to create a set of N_p PIPs, with $p = 1$ being either the shortest interframe time or largest window size, and $p = N_p$ being the longest time or smallest size.

1. A standard SPC algorithm is applied to the first set of images ($p = 1$).

2. If, based upon this initial displacement estimate, increasing the interframe time or decreasing the interrogation window size (incrementing the PIP to $p = 2$) will result in a displacement greater than one quarter of the window size, this initial estimate is used as the final displacement vector.

3. Otherwise, the $p = 2$ frame pair is partially processed; pausing after the SVD is performed. If the eigenvalue ratio is less than the threshold (defined below), the displacement estimate from the previous PIP is used as the final displacement vector.

4. If the eigenvalue ratio is above the threshold, the dominant mode is unwrapped and overlaid on top of the previous mode. The window size divided by 2π is used to scale the phase information such that the digital frequency ranges from $[-\pi, \pi]$.

5. Similarly, the RPC weighting function for data from each PIP must be scaled by the ratio between the interframe time at each additional framestep and the initial interframe time.

6. The weighted least squares regression is performed on the entire set of data using the scaled weighting functions, producing a new displacement estimation.

Steps 3, 4, 5, and 6 are repeated until either (a) the eigenvalue ratio drops below the threshold, (b) increasing the framestep will result in a displacement greater than one fourth of the window size, or (c) the user-specified maximum framestep is reached.

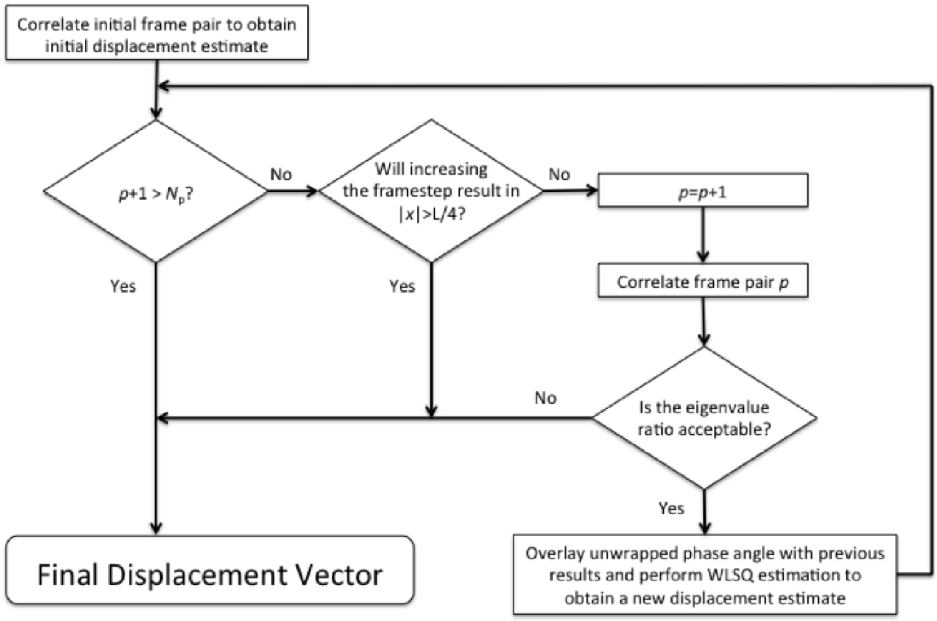

Figure 2.6: Flowchart illustrating the algorithm used in the ensemble multiframe/multiwindow SPC algorithm.

In order to eliminate the worst correlations while still keeping the method useful for experiments with high background noise, an arbitrary threshold of 1.5 was chosen for use in the ensemble algorithms, which seems to produce good results. This choice was motivated by the results plotted in Figure 2.5, where it can be seen that correlations with eigenvalue ratios below this threshold (plotted as the vertical blue dashed line) typically had high probabilities of failure (BVP). Other values provided similar results.

A method of weighting data from PIP's with higher quality was also tested. Following an analysis similar to that described in [16], the quality of each correlation was estimated from the eigenvalue ratio (ER), displacement magnitude (Δs), and uncertainty in the displacement estimation (σ_s) as:

$$Q_i = ER_i \left(1 - \frac{\sigma_s}{\Delta s_i}\right) \tag{2.8}$$

A value of 0.1 pix was selected for σ_s, although the analysis was found to be relatively insensitive to this parameter. The RPC weighting function for each correlation was normalized by:

$$w_i = \frac{Q_i - min\,(Q)}{max\,(Q) - min\,(Q)} \tag{2.9}$$

resulting in w_i ranging from 0 for the correlation with the lowest quality, to 1 for the correlation with the highest quality.

Traditional ensemble PIV averages correlations over the entire length of the experiment, which is trivial to implement with the SPC processor by overlaying the unwrapped phase information from each correlation before performing the weighted least squares regression. A weighted ensemble method was also tested, where the eigenvalue ratio of each correlation was used as the quality (Q) in Equation 2.9, since displacement should remain constant under steady flow conditions.

2.3.3 PIV Challenge Images

Images from Case B of the 2005 PIV Challenge [29] were used to evaluate the performance of the ensemble SPC algorithms against the standard SPC, as well as the SCC and RPC algorithms. The images were generated from a DNS simulation of a laminar separation bubble with a high VDR, under a degrading SNR. As in the uniform flow tests, the SCC algorithm used unfiltered 32x32 pixel windows, and the RPC and SPC algorithms used 64x64 Gaussian filtered windows with 32x32 pixel equivalent resolution. The multiframe SPC used up to four additional frame pairs ($N_p = 5$). The multiwindow SPC started with an initial equivalent window resolution of 64x64 pixels, with the possibility of including windows with 32x32 and 16x16 pixel equivalent resolutions to yield $N_p = 3$.

First, the ensemble methods were compared with a single-PIP SPC processing, and the effect of quality-based weighting of particle image pairs was examined. The relative error, $\Delta x'/\Delta x$, was computed for each measurement to produce the cumulative probability functions shown in Figure 2.7. These curves show the fraction of vectors with a relative error less than $\Delta x'/\Delta x$, meaning that perfect processing results would produce a step function.

The plot on the left was produced using data from the highest SNR image set, and the plot on the right from the lowest SNR set. At the high SNR, approximately 95% of the vectors from the single-PIP SPC method have a relative error less than 20%. The multiframe processing shows that relative error can be improved slightly with the addition of data with multiple interframe times. The multiwindow results show higher error levels, presumably due to data from the larger windows obscuring finer flow features. The addition of quality-based PIP weighting improved the multiwindow results significantly, and produced a slight improvement in the multiframe data.

At the lowest SNR, 75% of the vectors from the single-PIP SPC processing had a relative error greater than 20%. Here, the multiwindow SPC showed a significant improvement over results from the single-PIP and multiframe SPC, with more than twice as many vectors having a relative error less than 20%. This is likely due to the increased correlation SNR caused by the addition of larger windows, and is similar to the results of Theunissen et al. [30] where inhomogeneous window sizing resulted in fewer outliers in image regions with a low SNR. Quality-based weighting had essentially no effect on the multiframe or multiwindow results at the lowest SNR. This may be a result of the eigenvalue ratio may becoming a poor indicator of quality relative to other PIP's. Note that the steep decline in BVP with increasing eigenvalue ratio seen in the left side of Figure 2.5 is not as pronounced at low eigenvalue ratios.

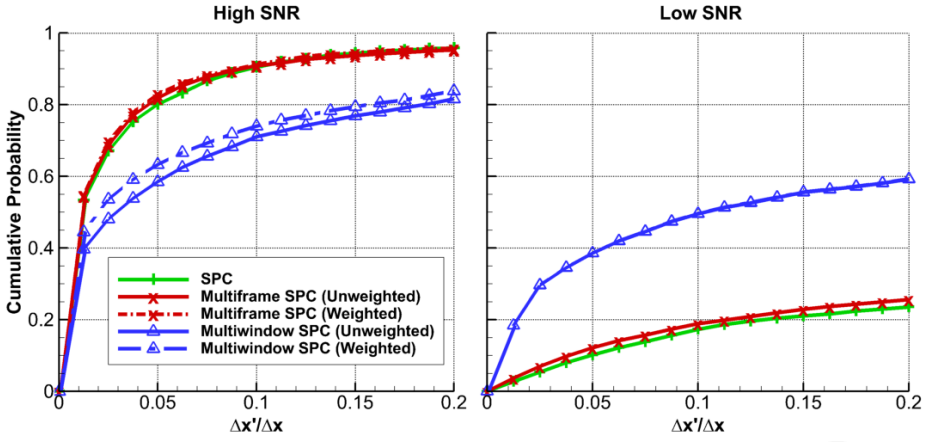

Figure 2.7: Cumulative probability functions for relative error on the PIV Challenge data for the highest SNR case (left) and lowest SNR case (right), examining the effect of quality-based PIP weighting on the SPC processing methods.

Discrete Window Offset (DWO) is a method commonly used to decrease error in PIV processing, which uses displacement results from an initial processing pass to initialize the search regions on an additional pass [31]. This results in a higher number of common particle images between frames (NF_iF_o), and a more refined estimate of displacement. The results presented in Figure 2.8 show a significant improvement in the single-PIP and multiframe SPC results at a low SNR. However, the DWO produces slightly worse results at a high SNR. This is likely an effect of not removing bad measurements between passes, as a poor velocity estimate on the initial pass will propagate into the second pass and degrade the estimate further. Detection of these bad vectors in experimental data is beyond the scope of this study, but the increase in performance at high noise levels even with no outlier detection justifies the inclusion of DWO in the algorithms. DWO had little effect on the multiwindow results, where the inclusion of a larger window size results in a higher NF_iF_o on the initial pass.

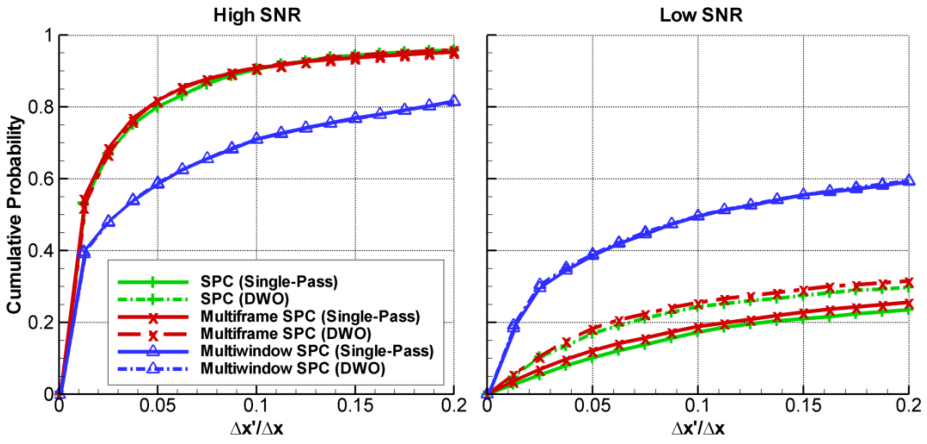

Figure 2.8: Cumulative probability functions for relative error on the PIV Challenge data for the highest SNR case (left) and lowest SNR case (right), examining the effect of discrete window offset (DWO) on the SPC processing methods.

The multiframe and multiwindow SPC methods incorporating quality-based weighting of the PIP's and DWO were compared with SCC DWO, RPC DWO, and single-PIP SPC DWO methods (with identical window sizes on both passes). The results in Figure 2.9 show that at high image SNR, the SPC and multiframe SPC performed comparably to the RPC, and much better than the SCC. The multiwindow SPC performed worse than the SCC, due to the larger window size obscuring finer features of the flow. As in the tests on uniform flow

data, images with a low SNR proved to be problematic for the SPC methods due to difficulty unwrapping the aliased phase information under high noise levels. At the lowest image SNR, both the multiframe and standard SPC performed much worse than the SCC or RPC. The multiwindow SPC performed better than the SCC, SPC, and multiframe SPC, and had the highest amount of vectors with a very low relative error, but did worse than the RPC overall.

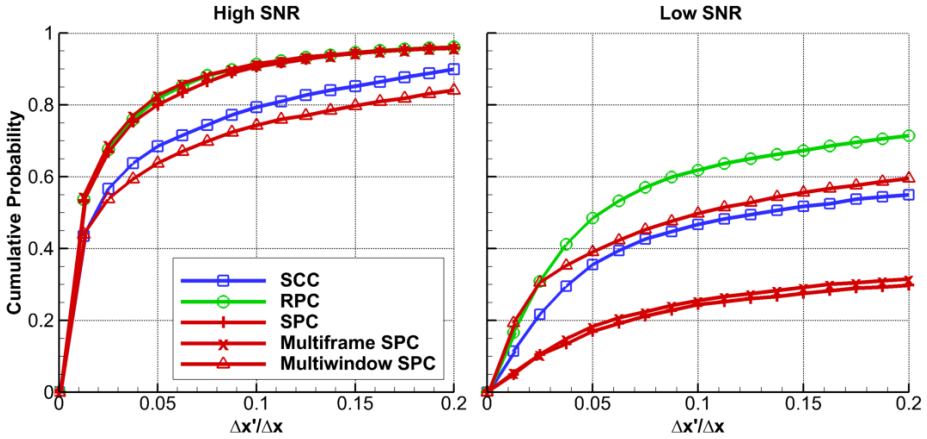

Figure 2.9: Cumulative probability functions for relative error on the PIV Challenge data for the highest SNR case (left) and lowest SNR case (right).

2.3.4 Rising Bubble Experiment

The single-PIP SCC, RPC, SPC, and multiframe SPC were also applied to real-world data of a bubble rising through quiescent water [32]; an experiment with a very high VDR due to high velocities near the interface and low velocities in the far-field. The images were evaluated with a two-pass DWO algorithm using Gaussian filtered windows with a 32x32 pixel equivalent window size on a 16x16 pixel grid on both passes. The flow was sampled at $750Hz$ ($\Delta t_2 = 1.33ms$) with $200\mu s$ between image pairs (Δt_1). Note in Table 2.1 that at the maximum frame step of $N_p = 5$, the interframe time ($5.53ms$) is almost twenty-eight times as long as the interframe time for the initial PIP ($0.2ms$).

As seen in Figure 2.10, which shows the RPC results on the left side of the bubble and the weighted multiframe SPC on the right side, the multiframe algorithm produces vectors which are significantly more uniform; both in magnitude and direction. The local variation in the velocity field ($|\mathbf{r}|$) was quantified by computing the absolute deviation between each velocity

Table 2.1: Possible PIP's and corresponding interframe times for the multiframe SPC algorithm in the rising bubble experiment.

PIP	**Timesteps**	**Interframe Time (ms)**
$p = 1$	Δt_1	0.20
$p = 2$	$2\Delta t_2 - \Delta t_1$	2.47
$p = 3$	$2\Delta t_2 + \Delta t_1$	2.87
$p = 4$	$4\Delta t_2 - \Delta t_1$	5.13
$p = 5$	$4\Delta t_2 + \Delta t_1$	5.53

measurement and the median of the remaining eight vectors in a 3x3 window surrounding each measurement. Instantaneous results comparing the local deviation of the RPC with the multiframe SPC processing are presented in Figure 2.11. The results of all methods were averaged temporally over the 110 frames of experimental data, as well as along the Y-axis to produce the curves shown in Figure 2.12. The single-PIP SPC method produces higher local variations than the CC-based methods, presumably due to the SPC's increased random error at higher noise levels (as seen in the uniform flow data). In the high velocity region near the bubble, located between approximately $X = -1$ and $1mm$, the multiframe SPC produces slightly higher local deviations than the RPC, on the same level of those produced by the SCC. However, the multiframe SPC shows a decrease in local deviation of up to an order of magnitude in the low-velocity far-field regions. It is noted that image windows on the left side of the bubble tended to contain a lower SNR due to a shadow cast as the bubble moved through the image frame. This does not appear to have caused a significant asymmetry in the SCC or RPC results, but the SPC's susceptibility to noise results in higher local deviations on the left side of the bubble as compared to the right.

2.3.5 Microchannel Poiseuille Flow Experiment

Experimental data from a μPIV experiment [33] was used to analyze the convergence of the SPC to a mean solution. The experiment consisted of steady Poiseuille flow through a rectangular microchannel of width $100\mu m$, depth $24\mu m$, and length $15mm$. In the test case

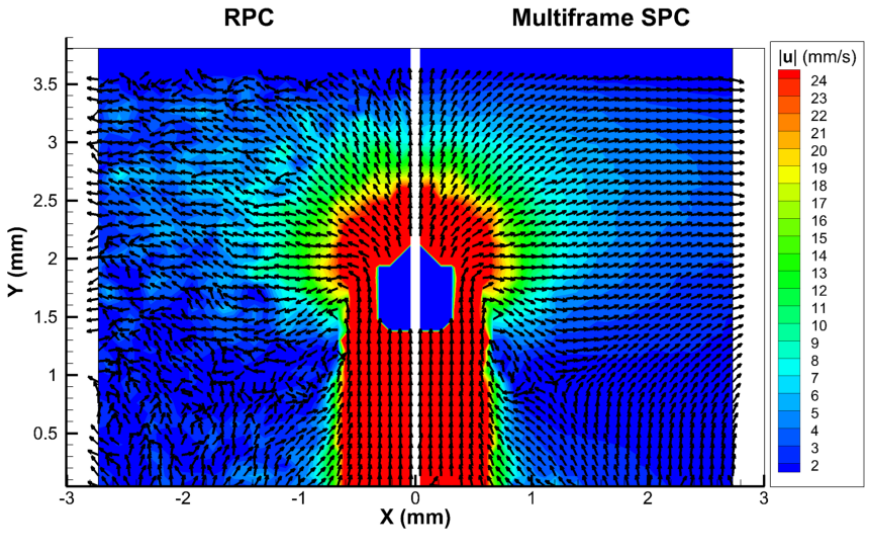

Figure 2.10: Experimental data processed using the RPC algorithm (left half) and the multiframe SPC algorithm (right half), contoured by velocity magnitude. The RPC results are from the right half of the experimental field of view, but have been mirrored over the bubble centerline

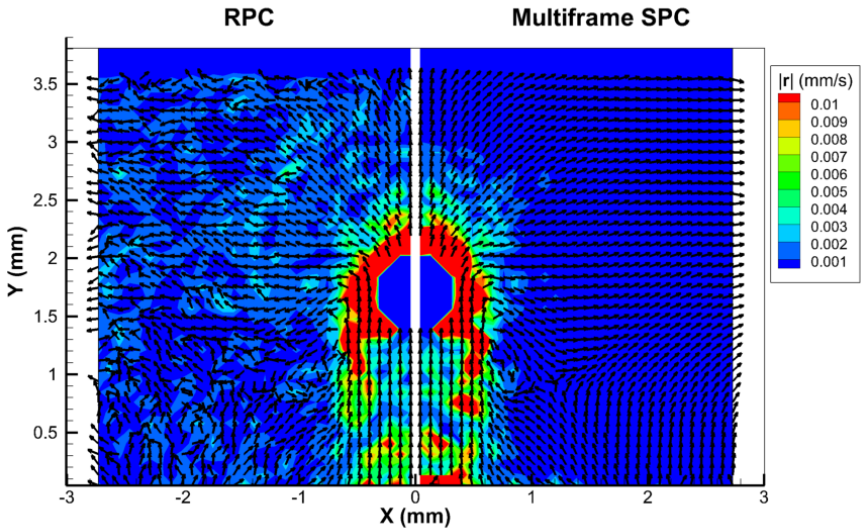

Figure 2.11: Experimental data processed using the RPC algorithm (left half) and the multiframe SPC algorithm (right half), contoured by local deviation. The RPC results are from the right half of the experimental field of view, but have been mirrored over the bubble centerline

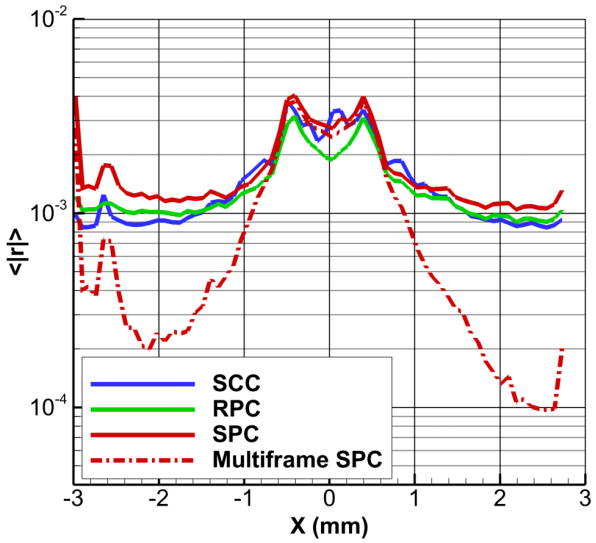

Figure 2.12: Mean local deviation over the length of the rising bubble experiment, averaged along the vertical axis for various processing methods.

analyzed here, the volume fraction of particles was 0.30%, and the objective was positioned such that its focal plane was $3\mu m$ from the near-side wall. The images were evaluated using a single-pass algorithm with 32x32 pixel unfiltered windows for the SCC processor, and Gaussian filtered windows with an effective size of 32x32 pixels for the RPC and SPC processors. Results for various ensemble lengths, M, are presented in Figure 2.13. The instantaneous results ($M = 1$) appear very noisy across all processing methods, but increasing the ensemble length produces results that are significantly more uniform in magnitude and direction. Applying quality-based weighting to the SPC produces smoother results, which appear closer to the RPC results at $M > 1$ (note that for $M = 1$ the weighted and un-weighted SPC results are identical).

The convergence of each method to an ensemble solution after 250 frames was examined following an analysis similar to that in [34]. The data was divided into subset ensembles of length n, where n is less than the length of the total number of samples, M. The variance of the subset ensembles, $var\left\{\bar{U}_n\right\}$, was computed relative to the ensemble solution after $M = 250$ samples, $\bar{U}$:

$$var\left\{\bar{U}_n\right\} = \frac{1}{P}\sum_{p=1}^{P}\left[\left(\bar{U}_n - \bar{U}\right)^2\right]_p \tag{2.10}$$

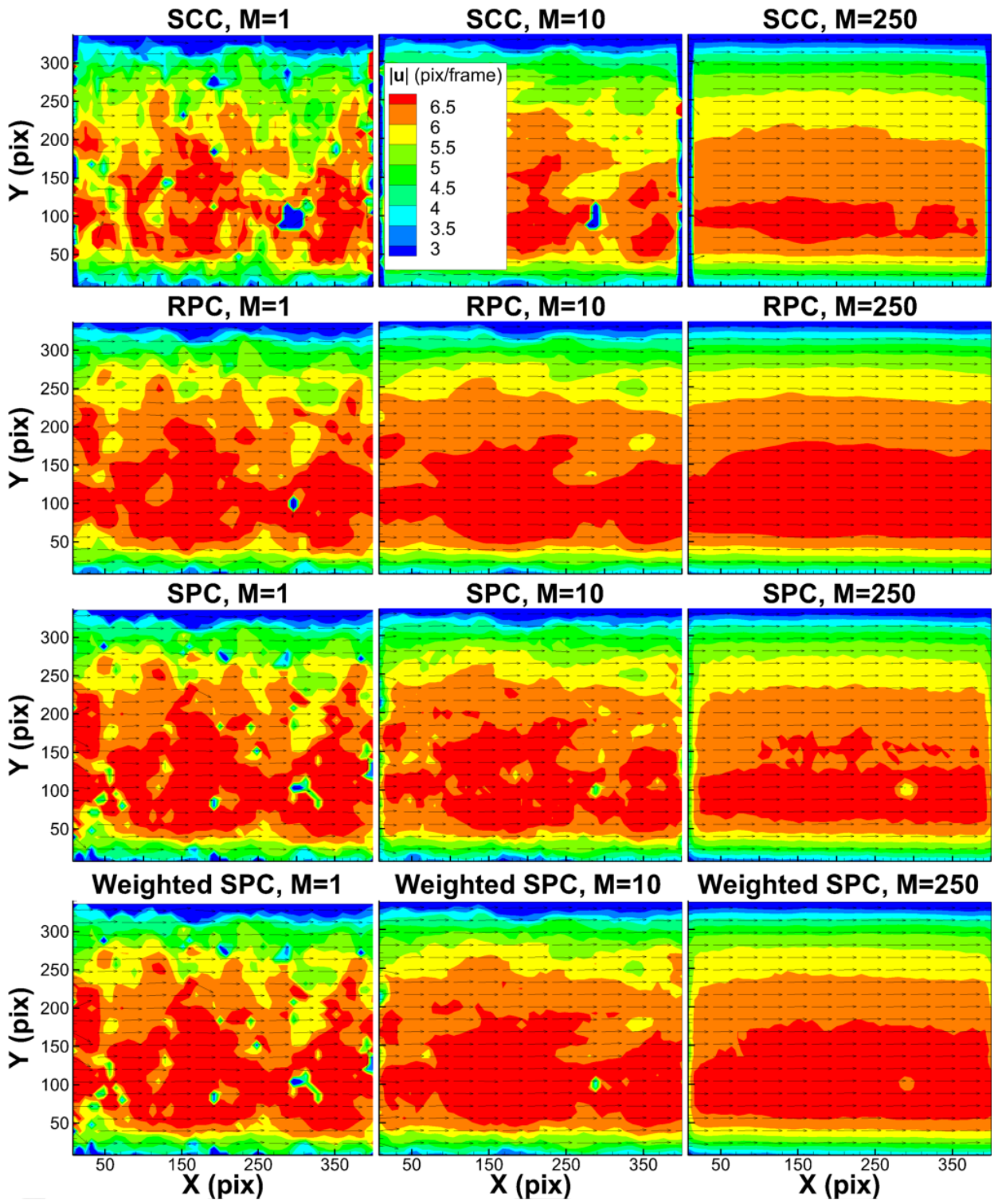

Figure 2.13: PIV results from the microchannel experiment for various ensemble lengths, M.

where P is the number of unique subset ensembles of length n that can be extracted from the available samples without repetition. Thus, Equation 2.10 provides a metric for quantifying the variance between ensembles of length n throughout the length of the experiment. If n is sufficiently large and the steady flow assumption is valid, the variance between ensembles should become very small.

Figure 2.14 shows the median variance over the streamwise velocity profile near the center of the measurement region, normalized by the square of each method's ensemble velocity profile. The curves approach zero as the number of samples in each sub-ensemble approaches $M = 250$. For small sample sizes, the variance of the SCC and RPC methods drops sharply with n, while the SPC without weighting sees a much slower decline. Across all sample sizes, the variance in the unweighted SPC measurements is much higher than that of the SCC and RPC measurements. However, quality-based weighting of the SPC measurements improves the results significantly; lowering the variance curve such that it drops sharply with n, and performs at the same level as the CC-based methods. It is noted that the μPIV images in this dataset have a low SNR, which resulted in poor SPC results in the uniform flow and PIV Challenge datasets. However, the weighted ensemble algorithm performs much better here, even under these high-noise conditions.

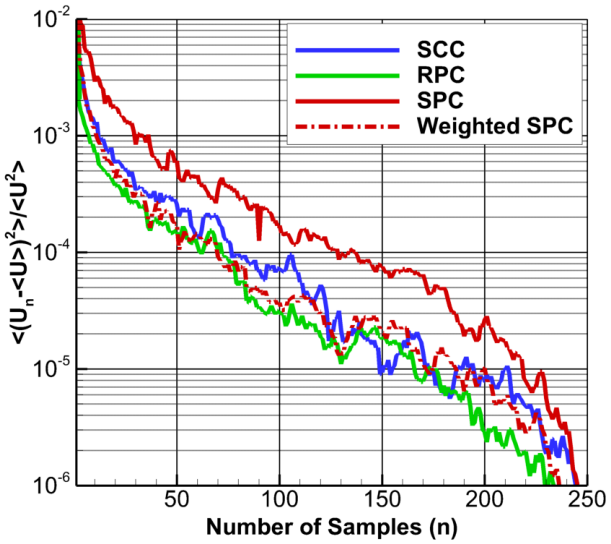

Figure 2.14: Median variance in the subset ensemble correlation for the microchannel velocity profile.

2.4 Conclusions

A novel PIV processing method was introduced that has multiple benefits over existing CC-based processing algorithms. The strengths and weaknesses of the method, and the effect of various modifications to the processing algorithm were investigated using a range of simulated images and experimental data.

The ability to obtain a displacement estimate while remaining in the Fourier domain opens up a new direction for PIV research. The novel SPC method allows for correlations with multiple interframe times and/or interrogation window sizes to be combined into a single displacement estimate, provides a metric for determining the quality of a correlation, and eliminates peak-locking errors introduced by spatial peak-finding algorithms in conventional PIV methods. In its current implementation, the SPC has been shown superior to standard PIV processing. Already, it performs at the same level as advanced cross correlation (CC)-based methods, but (unlike with CC-based methods) there is significant room for improvement. For instance, there may be a more robust method for decomposing the phase correlation matrix. The algorithm may also benefit from a more advanced method of unwrapping the dominant modes, or a two-dimensional unwrapping scheme that could create a displacement estimate directly from the phase matrix (thus eliminating the modal decomposition step).

Chapter 3

Contributions

An extensive set of shadowgraph and PIV experiments was performed on turbulent round gas jets submerged in water at jet speeds ranging from Mach 0.4 to Mach 2.1, with nozzle diameters of 3.175mm and 6.35mm. Liquid entrainment by each jet was measured and compared with two existing entrainment models:

1. *Ricou-Spalding [5]:* An empirical model developed through experiments performed on buoyant gas jets in a gaseous environment. Their linear relationship between jet flow rate and nondimensionalized axial distance is commonly used as an entrainment model in simulations of jetting flow. In this study, it is found to underestimate total entrainment by underwater gas jets, and does not predict the increase in entrainment coefficient with axial distance seen in the experimental results.

2. *Epstein et al. [11]:* A theoretical model developed for entrainment by underwater gas jets that assumes the entrainment process in dominated by a combination of Rayleigh-Taylor and Kelvin-Helmholtz instabilities growing on the gas-liquid interface. It requires jet properties as a function of height, rather than only conditions at the nozzle exit as in the Ricou-Spalding model. It was found to significantly overestimate entrainment in the present study, but correctly predicts an increase in entrainment rate with axial distance and decreasing jet speed, as is seen in the experimental results.

This study marks the first time underwater gas jets have been studied using PIV, and the first time the Epstein model has been compared to experimental entrainment rates in

underwater gas jets. While the Ricou-Spalding model has previously been compared with experimental studies on entrainment in gas jets, the PIV experiments in the present work provide significantly more data for comparison than previous experimental investigations.

A novel Particle Image Velocimetry (PIV) processing algorithm was introduced that is fundamentally different from existing PIV processing methods, opening up a new direction for future PIV research. The method's performance was demonstrated using artificial and experimental data. It was found to outperform the standard cross-correlation algorithm, and perform at the same level as the most advanced CC-based processing algorithm at low levels of background noise. It has the advantages over CC-based methods of (1) avoidance of errors introduced by spatial peak-finding routines; (2) use of a modal analysis that can be used to provide information such as correlation quality; and (3) introduction of a means of incorporating information from multiple image windows.

3.1 Publication List

The following publications have been produced based on the work presented in this thesis:

- B. P. Drew, J. J. Charonko, P. P. Vlachos. (2011). Liquid Entrainment by Round Turbulent Gas Jets Submerged in Water. ASME-JSME-KSME Joint Fluids Engineering Conference 2011. Hamamatsu, Shizuoka, Japan.
- J. J. Charonko, B. P. Drew, P. P. Vlachos. (2011). Enhancing the Velocity Measurement Dynamic Range Using Phase Correlation Particle Image Velocimetry (PIV). 9th International Symposium on Particle Image Velocimetry. Tsukuba, Japan.

Bibliography

[1] C. J. Weiland, "Characteristics of the high speed gas-liquid interface," Ph.D. dissertation, Virginia Tech, 2009.

[2] A. C. Eckstein and P. P. Vlachos, "Digital particle image velocimetry robust phase correlation," *Measurement Science and Technology*, vol. 20, no. 5, 2009.

[3] B. R. Morton, G. Taylor, and J. S. Turner, "Turbulent gravitational convection from maintained and instantaneous sources," in *Proceedings of the Royal Society of London. Series A, Mathematical and Physical Sciences*, ser. 234. The Royal Society, 1955.

[4] B. R. Morton and A. Ibbetson, "Jets deflected in a crossflow," *Experimental Thermal and Fluid Science*, vol. 12, pp. 112–133, 1996.

[5] F. P. Ricou and D. B. Spalding, "Measurements of entrainment by axisymmetrical turbulent jets," *Journal of Fluid Mechanics*, vol. 11, no. 1, pp. 21–32, 1961.

[6] B. J. Hill, "Measurement of local entrainment rate in the initial region of axisymmetric turbulent air jets," *Journal of Fluid Mechanics*, vol. 51, no. 4, pp. 773–779, 1972.

[7] J. C. Weimer, G. M. Faeth, and D. R. Olson, "Penetration of vapor jets submerged in subcooled liquids," *AIChE Journal*, vol. 19, pp. 552–558, 1973.

[8] S. R. Tross, "Characteristics of a turbulent two-phase submerged free jet," Master's thesis, Pennsylvania State University, 1974.

[9] B. R. Morton, "Modeling fire plumes," in *Symposium (International) on Combustion*, ser. 10, 1965.

[10] E. Loth and G. M. Faeth, "Structure of underexpanded round air jets submerged in water," *International Journal of Multiphase Flow*, vol. 15, no. 4, pp. 589–603, 1989.

[11] M. Epstein, H. K. Fauske, S. Kubo, T. Nakamura, and K. Koyama, "Liquid entrainment by an expanding core disruptive accident bubble - a Kelvin/Helmholtz phenomenon," *Nuclear Engineering and Design*, vol. 210, pp. 53–77, 2001.

[12] Z. Dai, B. Wang, L. Qi, and H.Shi, "Experimental study on hydrodynamic behaviors of high-speed gas jets in still water," *Acta Mechanica Sinica*, vol. 22, pp. 443–448, 2006.

[13] M. Raffel, C. Willert, S. Wereley, and J. Kompenhans, *Particle Image Velocimetry*. Springer, 2007.

[14] A. C. Eckstein, J. J. Charonko, and P. P. Vlachos, "Phase correlation processing for DPIV measurements," *Experiments in Fluids*, vol. 45, pp. 485–500, 2008.

[15] A. C. Eckstein, J. J. Charonko, and P. P. Vlachos, "Assessment of advanced windowing techniquies for digital particle image velocimetry (DPIV)," *Measurement Science and Technology*, vol. 20, no. 5, 2009.

[16] T. Persoons and T. S. O'Donovan, "High dynamic velocity range particle image velocimetry using multiple pulse separation imaging," *Sensors*, vol. 11, pp. 1–18, 2011.

[17] J. Westerweel and F. Scarano, "Universal outlier detection for PIV data," *Experiments in Fluids*, vol. 39, pp. 1096–1100, 2005.

[18] G. Berkooz, P. Holmes, and J. L. Lumley, "The proper orthogonal decomposition in the analysis of turbulent flows," *Annual Review of Fluid Mechanics*, vol. 25, pp. 539–575, 1993.

[19] E. Loth, "Study of underexpanded turbulent air jets in water," Ph.D. dissertation, University of Michigan, 1988.

[20] M. A. R. Talaia, "Terminal velocity of a bubble rise in a liquid column," *Engineering and Technology*, vol. 4, pp. 264–268, 2007.

[21] K. Ito, S. Kobayashi, and M. Tokuda, "Mixing characteristics of a submerged jet measured using an isokinetic sampling probe," *Metallurgical Transactions*, vol. 22B, pp. 439–445, 1991.

[22] R. D. Keane and R. J. Adrian, "Optimization of particle image velocimeters. I. double pulsed systems," *Measurement Science and Technology*, vol. 1, pp. 1202–1215, 1990.

[23] J. Kriegseis, T. Dehler, M. Gnirss, and C. Tropea, "Common-base proper orthogonal decomposition as a means of quantitative data comparison," *Measurement Science and Technology*, vol. 21, 2010.

[24] H. S. Stone, M. T. Orchard, E. Chang, and S. A. Martucci, "A fast direct Fourier-based algorithm for subpixel registration of images," *IEEE Transactions on Geoscience and Remote Sensing*, vol. 39, pp. 2235–2243, 2001.

[25] A. C. Eckstein, "Development of robust correlation algorithms for image velocimetry using advanced filtering," Master's thesis, Virginia Tech, 2007.

[26] R. Hain and C. J. Kähler, "Fundamentals of multiframe particle image velocimetry (PIV)," *Experiments in Fluids*, vol. 42, pp. 575–587, 2007.

[27] J. G. Santiago, S. T. Wereley, C. D. Meinhart, D. J. Beebe, and R. J. Adrian, "A particle image velocimetry system for microfluidics," *Experiments in Fluids*, vol. 25, pp. 316–319, 1998.

[28] E. Delnoij, J. Westerweel, N. G. Deen, J. A. M. Kuipers, and W. P. M. van Swaaij, "Ensemble correlation PIV applied to bubble plumes rising in a bubble column," *Chemical Engineering Science*, vol. 54, pp. 5159–5171, 1999.

[29] M. Stanislas, K. Okamoto, C. J. Kähler, J. Westerweel, and F. Scarano, "Main results of the third international PIV challenge," *Experiments in Fluids*, vol. 45, pp. 27–71, 2008.

[30] R. Theunissen, F. Scarano, and M. L. Riethmuller, "An adaptive sampling and windowing interrogation method in PIV," *Measurement Science and Technology*, vol. 18, 2007.

[31] J. Westerweel, D. Dbiri, and M. Gharib, "The effect of discrete window offset on the accuracy of cross-correlation analysis of digital PIV recordings," *Experiments in Fluids*, vol. 23, pp. 20–28, 1997.

[32] M. R. Brady, "Multiphase hydrodynamics in flotation systems," Ph.D. dissertation, Virginia Tech, 2009.

[33] S. A. Klein and J. D. Posner, "Improvement in two-frame correlations by confocal microscopy for temporally resolved micro particle imaging velocimetry," *Measurement Science and Technology*, vol. 21, 2010.

[34] N. E. Murray and L. S. Ukeiley, "An application of gappy POD - for subsonic cavity flow PIV data," *Experiments in Fluids*, vol. 42, pp. 79–91, 2007.